2020

Optimization Studies for the Gas Atomization and Selective Laser Melting Processes of Al10SiMg alloy

Sharon Park
University of Central Florida

OPTIMIZATION STUDIES FOR THE GAS ATOMIZATION AND SELECTIVE LASER MELTING PROCESSES OF Al10SiMg ALLOY

by

SHARON MI PARK
B.S. University of Central Florida, 2019

A thesis submitted in partial fulfillment of the requirements
for the degree of Master of Science
in the Department of Materials Science and Engineering
in the College of Engineering and Computer Science
at the University of Central Florida
Orlando, Florida

Summer Term
2020

ABSTRACT

Selective laser melting (SLM) is an additive manufacturing technology that can fabricate complex engineering components using a scanning laser beam to melt consecutive layers of powders with characteristics that significantly influence material properties. Present work investigates both the gas atomization and SLM processes for the Al10SiMg alloy with a focus on establishing the relationships among atomization parameters, powder characteristics, SLM parameters and material properties. Al10SiMg alloy powders (Al-10wt.%Si-0.5wt.%Mg) were batch-produced through gas atomization by systematically varying the melt flow rate (0.012 – 0.037 kg/s), gas pressure (1.4 – 3.1 MPa), and melt temperature (850 – 1000°C). The highest yield of 80 wt.% was accomplished for powders with particle size smaller than 75µm, considered suitable for SLM, utilizing gas pressure of 2.7 MPa, melt flow rate of 0.020 kg/s, and melt temperature of 950°C. Investigations for the SLM process were carried out to identify the optimal particle size distribution (PSD) and critical reuse limit for Al10SiMg powders. Five distribution ranges ($\leq$ 45µm, 20µm $\leq x <$ 63µm, $\leq$ 75µm, $\leq$ 106µm, 75µm $\leq x <$ 106µm), and five sets of recycled powder (new, one, five, ten and over twenty uses) were used to build SLM samples for metallographic and mechanical characterization. Archimedes' method, optical, scanning electron microscopy and mechanical testing in tension were employed to assess the influence of powder feedstock on part density, microstructure and mechanical properties, respectively. All particle size distributions examined in this study produced samples with over 99% relative density, but samples built with size range of 75µm $\leq x <$ 106µm yielded the highest tensile and yield strengths of 448 MPa and 265 MPa, respectively. Results from recycling demonstrated that Al10SiMg alloy powders can be reused in SLM without sacrificing quasi-static tensile properties.

The author would like to dedicate this work to her family, close friends, and colleagues that have supported and guided her throughout her years at the University of Central Florida and will undoubtedly continue to do so through the years to come.

ACKNOWLEDGMENTS

I would like to express my deepest gratitude to those individuals who facilitated my growth as a scientist and person during my undergraduate and master's study at the University of Central Florida (UCF). First, I am deeply indebted to my advisor Dr. Yongho Sohn for his years of mentorship, support and guidance during my undergraduate and master's degrees at UCF. In addition to my advisor, I would also like to thank my thesis committee members: Dr. Linan An, Dr. Yuanli Bai, and Dr. Swaminathan Rajaraman for their encouragements and valuable guidance.

At this time, I would also like to extend my sincere thanks to my fellow colleagues for their endless help, support, and friendship in the laboratory. Special thanks go to Dr. Le Zhou for lending his expertise in Transmission Electron Microscopy (TEM) and for years of mentorship and guidance in the lab. Special thanks are also extended to Mr. Edward Dein for his years of hands-on training, guidance and overall technical support in the laboratory. Additionally, I have great appreciation for the staff of the Materials Characterization Facility at UCF for their technical support and their efforts in upkeeping the equipment that was utilized to carry out the work for this thesis. I also want to express my sincere gratitude to Mr. Kyu Cho and Dr. Brandon McWilliams at the US Army Research Laboratory for their financial support and technical collaboration.

Lastly, I would like to thank my family and friends for their endless support and patience.

TABLE OF CONTENTS

LIST OF FIGURES

LIST OF TABLES

LIST OF ACRONYMS/ABBREVIATIONS

AM	Additive Manufacturing
CCGA	Close-coupled Gas Atomization
ED	Energy Density
EELS	Electron Energy Loss Spectroscopy
OM	Optical Microscopy
(L)PBF	(Laser) Powder Bed Fusion
PSA	Particle Size Analysis
PSD	Particle Size Distribution
SADP	Selected Area Diffraction Pattern
SDAS	Secondary Dendrite Arm Spacing(s)
SLM	Selective Laser Melting
SEM	Scanning Electron Microscopy
SLM	Selective Laser Melting
TEM	Transmission Electron Microscopy
UTS	Ultimate Tensile Strength
VH	Vickers Hardness
Y75, Y45	Yield for Powders less than 75 µm, 45 µm respectively
YS	Yield Strength

CHAPTER 1: INTRODUCTION

1.1 General Background

Close-coupled gas atomization (CCGA) is a popular method utilized for the production of metal powders. During the CCGA process, a molten metal flow is poured through a nozzle or orifice into an atomization chamber where the melt is atomized by rapidly flowing inert gas. CCGA occurs in two regimes, primary and secondary breakup [1]. Primary melt breakup is initiated when the gas flows interact with the melt near the entry point of molten metal into the atomization chamber. These gas flows cover the molten metal to break apart the liquid stream into fine droplets through rapid solidification. Small liquid droplets solidify into spherical powders in the primary breakup regime. Larger droplets and ligaments solidify further downstream in the secondary regime of breakup in gas atomization [2]. Following both primary and secondary breakup, metal powders are then extracted from a collection chamber.

Metallic powders produced by gas atomization have many applications including powder metallurgy, thermal surfacing and industrial component manufacturing. One surging application of gas atomized powders is in the field of additive manufacturing (AM). Laser powder bed fusion (LPBF) AM utilizes a laser beam to fuse layers of metal powders, termed powder bed, to effectively build engineering components layer by layer. This process eliminates many constraints of conventional manufacturing techniques and allows for enhanced flexibility in the design of engineering components. However, the quality of components manufactured by LPBF is highly dependent on the quality of the powders utilized in the process, among other parameters.

Selective laser melting, a LPBF AM technique, more colloquially referred to as metal 3D printing, is a disruptive manufacturing technology. This process utilizes a laser beam to fuse layers of metal powders and is commonly known as laser powder bed fusion (LPBF). Generally, the most influential LPBF processing parameters are laser power (W), laser scan speed (mm/s), slice thickness (mm), i.e., powder-bed or layer thickness, and hatch spacing (mm), i.e. distance between adjacent laser scans. These parameters can be normalized as volumetric energy density (ED). ED is defined in Eq. (1) and is often correlated to many characteristics of microstructure, properties and thermo-physical phenomena associated with SLM.

$$\text{Energy Density (ED)} = \frac{\text{Power}}{\text{Scanning Speed} \times \text{Hatch Spacing} \times \text{Slice Thickness}} \quad (1)$$

1.2 Motivation

Powder feedstock characteristics and quality are integral components to the successful application of SLM technology. Therefore, it is critical to identify the optimal particle size distribution and determine the reusability of powder feedstock. Furthermore, it is important to develop an understanding of how to optimize the gas atomization process and tailor the atomization parameters to efficiently produce powder feedstock suitable for AM processes. Following production of powder feedstock and subsequent manufacturing via AM, components must be qualified for use in industrial applications. Qualifiable AM components are typically identified on the basis of full density, crack free specimens that have required (mechanical) properties which are investigated for the Al10SiMg alloy in this thesis.

1.3 Objective

In this thesis, correlations among gas atomization parameters, alloy powder characteristics, SLM parameters and microstructural and mechanical properties were examined for Al10SiMg alloys. This thesis was carried out through three projects: (1) Parametric Study of Gas Atomization for Powder Processing, (2) Effects of Powder Size Distribution on SLM Parts, and (3) Powder Recycling Effects on SLM Parts. First, extensive parametric studies were conducted to optimize the gas atomization process for efficient, AM-tailored production of Al10SiMg powder feedstock. Gas atomization parameters varied in this study were melt flow rate, atomizing gas pressure and melt temperature. Second, various particle size distributions were collected from gas atomization experiments and employed to build Al10SiMg alloy samples to determine the optimal distribution that results in the most dense, least porous and mechanically robust as-printed samples. Finally, new and "recycled" powder feedstock were used to build a variety of samples to identify the critical reuse limit of Al10SiMg powder feedstock in the SLM process, based on microstructure and mechanical properties.

CHAPTER 2: LITERATURE REVIEW

2.1 The Al10SiMg Alloy

Aluminum alloys are well-established and highly utilized in industrial applications due to superior characteristics which include ductility, weldability and high strength to weight ratios. Typical alloying elements include silicon, magnesium, manganese, tin, copper and zinc [3]. Aluminum alloys are generally classified under two categories – cast alloys and wrought alloys. While cast aluminum alloys exhibit lower tensile strengths than wrought, they tend to be more cost-effective and can be produced at lower melting points [4]. The AlSi binary alloy system, the primary system in the Al10SiMg alloy, is arguably the most common cast aluminum alloy. Examining the solidification behavior and microstructure arrangement of the binary Al-Si and Al-Mg systems that make up the ternary Al-Si-Mg system will aid in analysis of Al10SiMg following the atomization and SLM processes. Therefore, before discussing the Al10SiMg alloy, it is first important to understand the binary system behavior between Al and Si as well as Al and Mg.

The Al-Si binary system is a simple eutectic system which has provided significant commercial contributions to the automotive and aerospace industries [5]. This system is commonly utilized to develop more complex Al alloys and understand their behavior. The two constituent phases in this system are both solid solutions where Al has a face centered cubic (FCC) structure and Si has diamond cubic structure. The melting points of Al and Si are 660°C and 1414°C, respectively. While Si is a common impurity found in most aluminum alloys, it is often utilized as a major alloying addition in both wrought and cast aluminum alloys [6]. Typical cast aluminum alloys will contain anywhere from 5 to 22 wt.% Si [7]. This composition range results in the improvement of the fluidity and castability of aluminum by Si [8]. Addition of Si in Al also reduces

shrinkage which reduces strain levels and reduces the likelihood of the alloy cracking during solidification. The binary Al-Si phase diagram is presented in Figure 1 and was first studied in 1908 by a German scientist named Fraenkel. At room temperature, there is virtually no solubility for Si in Al and vice versa. Under equilibrium conditions, the terminal solid solutions are nearly pure Al and Si. In the phase diagram, a eutectic reaction is identified at 12.6 wt.% Si and 577°C. At this eutectic temperature, the maximum solubility of Si in Al occurs at 1.65 wt.%.

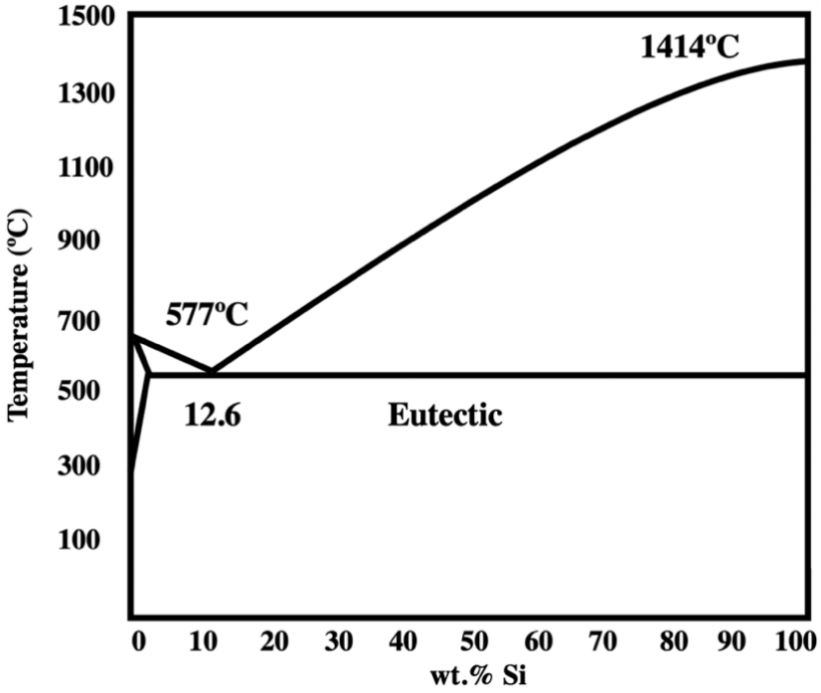

Figure 1. Binary Al-Si phase diagram *[9]*

When Cu and Mg are alloyed to the Al-Si system, intermetallic phases such as magnesium silicide (Mg_2Si) and aluminum copper (Al_3Cu) can form. These phases can improve the mechanical properties of the alloy and allow for successful heat treatment. The microstructure of these alloys will also contain primarily α-Al dendrites and eutectic Si particles [10].

Similar to Al-Si, Al-Mg binary alloys have been widely utilized in industry due to their beneficial material properties, namely, excellent corrosion resistance [11]. More specifically, Al-Mg alloys have been utilized as matrix alloys for composite materials as result of their low density and high wettability [12]. Additionally, the low melting point of this system leads to use of Al-Mg for a variety of casting applications. Al-Mg alloys (5000 series) with less than 5 wt.% Mg are utilized as wrought alloys whereas compositions of 5 – 10 wt.% are used as casting alloys [13]. The binary Al-Mg phase diagram is presented in Figure 2. The equilibrium phases of this binary system near the pure Al and Mg ends, are the FCC solid solution Al phase and the hexagonal close packed (HCP) solid solution Mg phase. At room temperature, the solubility of Mg in FCC Al is less than 1 wt.%, however at higher temperatures, i.e. 400°C the solubility increases to 15 wt.%.

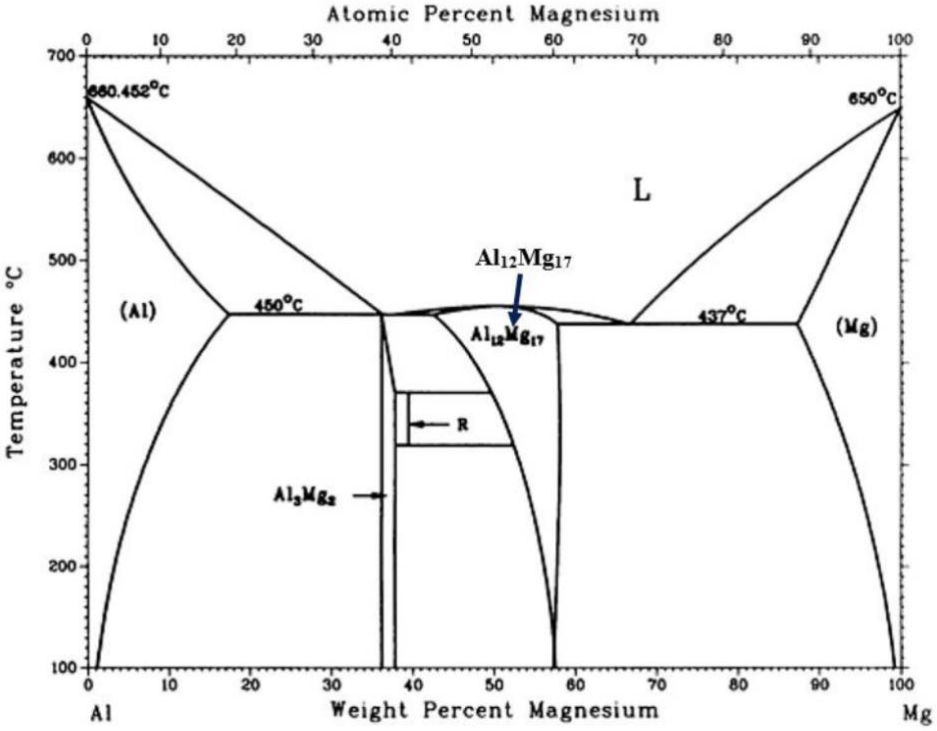

Figure 2. Binary Al-Mg phase diagram *[14]*

Both the Al-Si and Al-Mg systems have independently warranted extensive research and adaptation into industrial practice. Moreover, the ternary Al-Mg-Si system is also being increasingly utilized for many similar properties exhibited by the binary Al-Mg and Al-Si systems with the added benefit of traits like low hot tearing tendency [15].

The Al10SiMg alloy, a traditional hypoeutectic cast alloy, is one example from the Al-Si-Mg ternary alloy system which holds great prominence in the AM community [16]. Currently, the arsenal of Al alloys available for use in AM is slim. This is due to a host of factors, from high reflectivity of Al, low viscosity of molten Al (leading to poor flowability) and strong tendency to form oxides [17]. However, of the limited number of Al alloys available for AM, Al10SiMg is the most dominant. Popularity of the Al10SiMg alloy for AM purposes can be attributed to its near-eutectic composition which decreases the melting range and increases hot tearing resistance, while maintaining ductility. The nominal composition of this alloy is presented in Table 1.

Table 1. Nominal composition of Al10SiMg alloy *[18]*

Element	**Mass (%)**
Aluminum	Bal.
Silicon	9.00 – 11.00
Magnesium	0.25 – 0.45
Iron	< 0.25
Nitrogen	< 0.20
Oxygen	< 0.20
Titanium	< 0.15
Zinc	< 0.10
Manganese	< 0.10
Nickel	< 0.05
Copper	< 0.05
Lead	< 0.02
Tin	< 0.02

This alloy is primarily composed of Al, Si and Mg, with trace impurities. The addition of 0.5 wt.% Mg to the Al-Si binary system results in the formation of Mg_2Si precipitates. However, these precipitates are not commonly observed in the as-built condition. This is due to the high solidification rates associated with the SLM process. In lieu of these precipitates, cellular boundaries that are rich in Si occur in the as-built state [19]. Further development, i.e., heat treatment, can result in the formation of needle-like Mg_2Si precipitates [16] which commonly increase the strength of the alloy. Although heat treatments of Al10SiMg were not explored in this thesis, this research area is of great interest for AM technology.

2.2 Gas Atomization

Origins of gas atomization technology can be traced back to the World War II era, when a German scientist named R.Z. Mannesmann pioneered a "two-liquid" novel atomization method for iron powder production [20]. Following invention, early development of gas atomization technology was popularized by the chemical processing industry for atomization of liquids such as slurries, gels, oils and emulsions [20]. By the 1960's this technology was further advanced, and inert gas atomization was adopted for a wide range of materials to be utilized in aerospace applications. Being the most common method of metal powder production, optimization of the gas atomization process is of particular interest to powder metallurgy and metal AM research even today. This optimization involves such research as computational fluid dynamics (CFD) simulations of melt breakup, and analysis of atomizer nozzle configuration [21].

In relation to the scope of this thesis, several parametric studies of the CCGA technique have been conducted. Ünal [22] observed various relationships between gas atomization

parameters, and particle size. In this study, a close coupled gas atomization system with annular nozzle was employed to atomize AA2014. This alloy was chosen for its low liquidus temperature (620°C) and for its nonreactive properties. Atomization was carried out utilizing varying flow rates, pressures and types of atomizing gas. To vary the melt flow rate, the purging gas over the melt was pressurized to maximum of 0.014 MPa which allowed the melt to pour through the nozzle at varying rates. This procedure was carried out for a range of melt flow rates from 0.3 – 2.0 kg/min. Selected results from melt flow rate experiments are detailed in Table 2.

Table 2. Particle size of powders produced by gas atomization using Nitrogen as atomizing gas at various pressures and flow rates reported by Ünal *[22]*

Pressure (MPa)	**Flow Rate (kg/min)**	**Mean Particle Diameter (μm)**
1.56	0.376	22.83 ± 3.40
	0.609	25.46 ± 3.84
	1.205	30.97 ± 6.52
1.05	0.678	39.15 ± 6.02
	0.850	42.47 ± 5.06
	1.080	51.08 ± 14.20
2.12	0.545	27.27 ± 6.18
	1.090	29.13 ± 7.09
	1.607	30.86 ± 7.71

Generally, an increase in melt flow rate was directly correlated to larger powder particles. According to the author, the particle size increased proportional to the square root of the melt flow rate [22]. Ünal also studied the effects of melt temperature on the atomization process. At all temperatures of the study, 775°C – 925°C, atomization occurred successfully, and results indicated that melt temperatures above 825°C led to minor powder refinement. Powders atomized at temperatures around 775°C were slightly coarser with a wider dispersion in particle size distribution. This was attributed to lower surface tension and viscosity of the melt [22].

A study by Janowski *et* al. [23] found no significant variations in powder characteristics as a function of backfill gas or atomizing gas. For this study, stainless steel 304L rods were gas atomized using Argon in five different atomization runs. Results were obtained by analyzing powder production at the same gas/metal flow rate ratios and indicated that higher gas pressures, around 2.12 MPa, did not produce finer powders than those powders produced with lower gas pressures, around 1.56 MPa [23]. These results demonstrate that gas pressure is not an independently influential parameter and does not have significant effects on the powder yield or particle size distribution. This study also examined the mechanical properties of nitrogenated stainless steel powders after hot isostatic pressing (HIP) consolidation. Authors noted varying amounts of internal porosities in powders were a result of differences in chemical behavior of the gas/metal system, and atomizing gas pressure. This observation was attributed to solubility of the atomizing gas in the liquid and solid metal. These results are similar to those found for the atomization of Rene-95 alloy by VanStone *et* al. [24].

Effects of processing parameters on the surface morphology of metallic powders was studied by Singh *et* al. [25]. Atomization in this study was conducted for aluminum, lead, zinc and

tin. Superheating of 70 – 190 K was applied, and its effects were analyzed with respect to powder morphology. At all superheat temperatures, except for 150 K, atomized powders display slightly irregular morphology with mostly rounded particles. For powders atomized at a superheat temperature of 150 K, most particles appear spherical with remaining particles exhibiting oblate shape. Authors explain these observations with respect to the relationship between superheat and viscosity. As superheat temperature increases, the material's viscosity will decrease, which causes a decrease in the spheroidization time of particles. Nichiporenko and Naida [26] have proposed equation (2) to calculate the time for spheroidization. The r_p is the radius of the droplet preceding spheroidization, and R_p is the radius following spheroidization. Additional studies like those conducted by See *et* al. [27] have shown that the shape of powder particles in gas atomization is driven by spheroidization and solidification.

$$t_{sph} = \frac{3\mu_m^2}{4V\sigma_m}(R_p^4 - r_p^4) \qquad (2)$$

As demonstrated in the studies discussed above, desired powder morphology and particle size can be achieved through identification of optimal gas atomization parameters. Furthermore, powder qualities like particle size and morphology are known to affect powder flowability, which can improve "spreadability" of powder bed for the SLM process. Generally, good "spreadability" is associated with good powder packing fractions, which can lead to high quality as-printed components. Therefore, in the following chapters, a parametric study for the gas atomization of Al10SiMg is presented and discussed with regards to applications in SLM.

2.3 Selective Laser Melting

SLM technology originated as a result of a research project conducted in 1995 at the Fraunhofer Institute (ILT) in Aachen, Germany. This project was conducted by German scientists Dieter Schwarze and Matthias Fockele in collaboration with ILT researchers Wilhelm Meiners and Konrad Wissenbach and resulted in the ILT SLM patent, #DE19649865C1 [28]. Although many researchers distinguish the SLM process from selective laser sintering (SLS), the ASTM International F42 standards committee has listed SLM into the category of "laser sintering" [29]. While similar, the two techniques differ in their materials processing, i.e., SLM is not a true sintering process, as it fully melts materials into homogeneous components. This distinction is important to note, as the solidification behavior, associated with liquefaction in SLM vs. unmelted particles in SLS, differs significantly in the two processes [30].

In many SLM research studies emphasis lies on qualities such as processing parameters, laser configuration, etc. While important, these factors often overshadow a critical driving force in SLM – powder feedstock. More specifically, powder feedstock particle size distribution has an integral role in the SLM process by determining the powder bed formation as well as powder packing [31]. These factors alone play a large role in the melt-laser interaction. Studies like those conducted by Yablokova *et* al. [32] have also shown that feedstock particle size has nontrivial effects on powder flowability. Flowability of powder feedstock effects a variety of factors in the SLM process, namely, feed rate of powder, spreadability of powders during recoating, and contact area between particles in the powder bed [33].

Riener *et* al. [34] recently conducted a study on the effects of particle size on Al10SiMg processed by LPBF. Powder feedstocks were labelled by authors as A1, A2, A3 and B1. These

feedstocks had average particle sizes of 45 µm, 31 µm, 37 µm, and 41 µm respectively. All powders were manufactured via gas atomization with the exception of powder sample B1, which was manufactured via plasma atomization – as a result feedstock B1 was shown to be significantly more spherical. However, in general, the particle morphology was found to be directly correlated to the particle size in that smaller particles were more spherical. Higher surface roughness values were also observed in samples which contained a large number of fine particles. Flowability of powder feedstock was measured via a revolution powder analyzer and characterized by avalanche angle, where a larger angle corresponds to a lower flowability. Powders with average particle size of 31 µm (A2) and 37 µm (A3) exhibited nearly identical avalanche angles, i.e., flowability, while 45 µm (A1) powder feedstock showed a higher flowability. Average particle size of 41 µm (B1) resulted in the highest flowability. Generally, increasing the powder feedstock particle size resulted in greater flowability, as was also shown in a study conducted by Pohlman *et* al. with titanium powder feedstock [35].

The laser absorption of powder samples was measured by ultraviolet-visible spectroscopy, and Reiner [34] found that the absorption values increased with larger amounts of fine powder in feedstock. Absorptivity was also found to increase with the presence of highly irregular shaped particles. Laser absorption was found to be a good indicator for powder layer density, which affects the subsequent as-printed component density. For fabrication of samples, laser parameters were kept constant with the exception of scan speed which varied from 1600 mm/s – 2400 mm/s in 200 mm/s intervals. Density of subsequent SLM components was measured via image analysis and values are listed in Table 3.

Table 3. Relative density for Al10SiMg manufactured via SLM with varying particle size *[34]*

Average Particle Size (µm)	**Component Density (%)**
41 (B1)	99.98 – 99.99
37 – 45	99.98 – 99.93
31	99.84 – 99.87

It is important to note that for all parameters and average particle sizes, the density of components exceeded 99.80% and the variation between density for all particle sizes was minimal. However, the authors [34] suggested that component density is linked to powder layer density, and that higher layer density produced higher component density. Powder layer densities were measured using a specialized test bench which simulated the recoating process and uses a cavity embedded into the build platform. Weights of the powder layer, W_1 and W_2 were measured before and after recoating, and the layer density was calculated according to equation (3), where V represents the known volume of the cavity and $\rho_M = 2.67$ g/cm^3, the material density of Al10SiMg.

$$\rho_L = \frac{(W_1 - W_2)}{V \cdot \rho_M} \cdot 100\% \qquad (3)$$

In decreasing order, the highest layer density values came from powder samples with average particle sizes of 41 µm (B1), 45 µm (A1), 37 µm (A3) and 31 µm (A2). Correlations between high layer density and high density sample were assumed on the basis of lower densification requirements for higher layer densities. Lastly, results from tensile testing are shown in Figure 3. As is depicted, particle size independently did not correspond to significant variations in yield strength (YS) or elongation for Al10SiMg. This was also the case for ultimate tensile

strength (UTS) values for this alloy as is shown in Figure 4. Rather, these results proved that laser scan speed was the most influential. Figure 3 illustrates the increase of YS with increasing scan speed. Buchbinder *et* al. [36] have shown that increasing scan speeds result in higher cooling rates and subsequently higher solidification rates. Based on Hall-Petch relation, the refinement in the microstructure from high solidification rate favors high YS [34]. Elongation values for this alloy and range of scan speeds depicts an opposite trend to that of the YS. Assumed increases of residual stresses with increasing scan speeds was used to justify the trend observed. Interestingly, these results also highlighted the effects of powder production on SLM component production. Riener *et* al. [34] noted that plasma atomized powders (B1) provided slightly higher elongation and UTS values. This was hypothesized to be the result of the spherical morphology and higher densities achieved from plasma atomized powders. However, this hypothesis was not proved in their study.

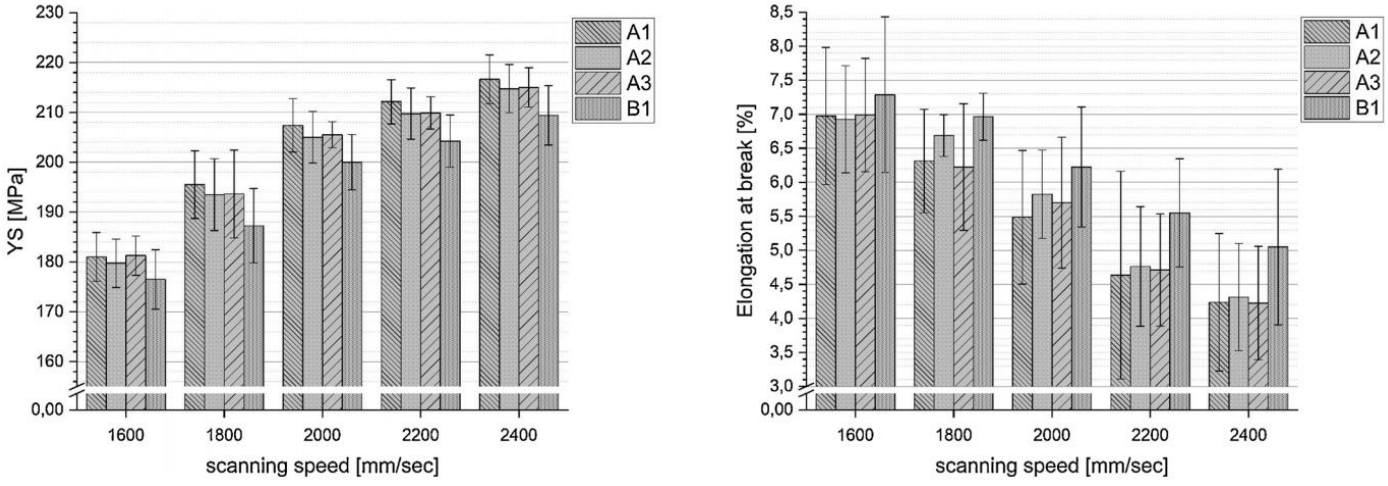

Figure 3. Yield strength and elongation values plotted for all samples *[34]*

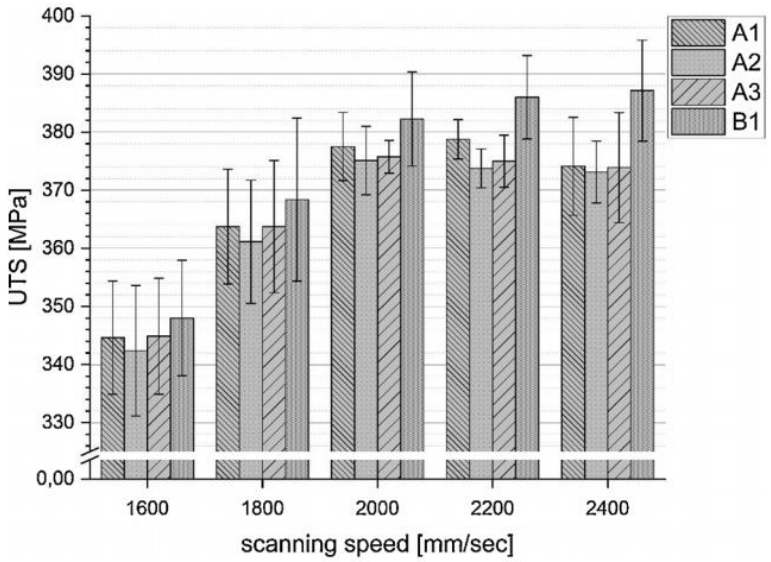

Figure 4. Ultimate tensile strength values for all powder samples and scan speeds *[34]*

Influences of particle size distribution was studied for the stainless steel 316L alloy by Spierings *et* al. [37]. Samples from three particle size distributions, with average particle size 15.12 μm, 28.26 μm, and 55.54 μm, respectively were manufactured via SLM. For this alloy, particle sizes 1 and 2 had comparable mechanical strength despite large difference in average particle size. However, particle size 3, which had the largest average particle size of 55.54 μm showed significantly less mechanical strength, which was attributed to a reduced thermal penetration depth. It was hypothesized that this reduced penetration depth prevented complete (re)melting of consecutive powder layers, which would lead to incomplete fusion of the component and reduced mechanical strength. Authors formulated equation (4) to show that larger particles require higher energy absorption, where C_p, L_m, A, I_0 and r represent specific and latent heat of fusion, absorption coefficient of powder, intensity of the laser beam, and particle radius respectively. The ratio of available energy to required energy needed to melt particles decreases as particle radius increases according to Eq. (4).

$$\frac{E_{av}}{E_{need}} = \frac{A \cdot I_0 \cdot \pi \cdot r^2}{\left(\frac{4}{3}\right) \pi \cdot r^3 \cdot \rho \cdot (C_p \Delta T_m + L_m)} \quad (4)$$

Another study conducted by Alfaify *et* al. [38] evaluated the effects of particle size distribution in the pulsed SLM process for the Ti64 alloy. For fabrication of the samples, a pulsed SLM system, i.e. pulsed, discrete wave emission rather than continuous wave, was utilized. For this mode of SLM, scan speed is calculated using equation (5) where point distance refers to distance between consecutive points, and jump speed refers to the speed at which the optics move when the laser is moving from point to point.

$$\text{Scan Speed} = \frac{\text{Point Distance}}{\text{Exposure Time} + \frac{\text{Point Distance}}{\text{Jump Speed}}} \quad (5)$$

Three particle size distributions with average particle sizes of 32 µm, 59.3 µm and 73.6 µm respectively were studied. Samples were built using these distributions coupled with a fixed jump speed of 5000 mm/s and variety of process parameters/exposure times. Alfaify *et* al. [38] found that the highest as-printed density was achieved using a combination of various parameters with an average particle size of 50 µm, hatch spacing of 65 µm, laser power of 200 W, slice thickness of 30 µm and exposure time of 50 µs [38]. However, authors note that while particle size distribution can independently affect resultant part density, manipulation of SLM parameters can provide optimal results when printing with varying particle size distributions.

With the increasingly rapid development of SLM technology, and many industrial sectors becoming “early adapters” for the use of metal AM, many researchers have also begun economic

sustainability studies of SLM. In particular, identifying the reuse/recycling limit of metal powders [39, 40, 41, 42] to reduce material waste and cost has become an important aspect of AM. These types of studies are important for the future widespread employment of AM technology in industry.

One such study conducted by Asgari *et* al [43] investigated the effects of recycled AlSi10Mg_200C powders on the microstructural and mechanical properties for the Direct Metal Laser Sintering (DMLS) process. The distinction "_200C" refers to EOS processed Al10SiMg powders which is specified for a build plate temperature of 200°C [44]. Notably, the average particle sizes of virgin powders and condensate powders, i.e., powders which were partially melted/heated in the process, differed significantly. Asgari *et* al utilized virgin Al10SiMg powder with average particle size of 8.8 ± 7.0 μm and found that condensate powders had an average particle size of 66.5 ± 11.0 μm [43]. Powder morphology was also found to vary slightly between virgin and condensate powders where condensate powders had more pronounced satellites and more irregularity in shape.

The mechanical properties of samples manufactured from recycled powders, however, were comparable to those manufactured with virgin powders. Asgari *et* al. [43] compared tensile properties of specimens manufactured using recycled Al10SiMg against a variety of other studies which manufactured Al10SiMg using virgin powders. In addition to recyclability, some of the studies observed the effects of build orientation. Build orientation, either horizontal or vertical, refers to the orientation of tensile specimen on the build plate during the SLM process. Some of these comparisons are tabulated in Table 4, where V represents laser scan speed. In addition to tensile testing, Asgari *et* al. [43] presents fracture surfaces of tensile specimen to observe fracture mode of samples. This work is not included in this discussion.

Table 4. Mechanical properties of Al10SiMg_200C alloy printed using virgin and recycled powders reported by various studies in literature

Ref.	Machine/ Powder	Power (W) / V (mm/s)	Build Orientation	YS (MPa)	UTS (MPa)	Elongation (%)
[43]	EOS M290/ Recycled	370/ 1300	Vertical	240	393	5.8
			Horizontal	210	386	8.8
[45]	Concept Laser M2/ Virgin	175/ 1025	Vertical	232	319	1.1
			Horizontal	252	339	1.3
[46]	Concept Laser M1/ Virgin	200/ 1400	Vertical	N.A.	396	3.5
			Horizontal	N.A.	391	5.6

While the results reported in Table 4 assess combined effects of powder recycling, laser parameters, build orientation, etc. on the tensile behavior of as-printed Al10SiMg, they provide a preliminary basis for the reasoning that powder feedstock can be reused, to a certain extent, without suffering detrimental effects on mechanical properties. However, the individual effects of powder recycling will be detailed further in this thesis.

Cordova *et* al. [47] tested the effects of reused powders on SLM components for four different alloys – Inconel 718 (IN718), Ti64, AlSi10Mg, Al-Mg-Sc (Scalmalloy). Virgin powders referred to powders received directly from the supplier, and not utilized previously. Recycled powders referred to powders that were utilized in the SLM powder for more than one build cycle (i.e., not fused within in the part). Powder morphology after recycling for all alloys exhibited noticeably more surface roughness and satellites. Out of all powder feedstock, AlSi10Mg powders had the largest increase in average particle size after reuse. Oxygen content of powder samples was determined via LECO chemical analyzer. Changes in oxygen content after reuse was not

appreciable for Ti64 and IN718. However, this was not the case for the aluminum alloys, in fact, the oxygen content for AlSi10Mg feedstock doubled from the initial value – which the author attributed to aluminum's readiness to form the Al_2O_3 oxide [48], element vaporization and contamination pick up during processing [47].

Effects of powder recycling on the tensile and fatigue behavior for Ti64 AM parts was studied by Carrion *et* al. [49]. Virgin powders were tested against recycled powders, which were defined as powders reused fifteen times, for the LPBF process. Negligible effects were found for the microstructure of components when using virgin vs. recycled powders. However, authors noted that particle size distribution was narrower and spherical morphology was preserved after continued reuse. Strain-controlled fatigue tests were conducted according to the ASTM E8 standard using an MTS extensometer with 10 mm gage length and strain rate of 0.001 s^{-1}. Most interesting results included the observation of significantly longer fatigue life for samples manufactured from used powder vs. those manufactured from virgin in high fatigue cycle regimes, i.e., $\varepsilon_\alpha = 0.004$ mm/mm [49]. Carrion *et* al. suggested that recycling powders may improve the fatigue resistance of LBPF Ti64 as a result of increased flowability and better powder packing observed for recycled powders. The authors postulated that such properties would lead to less internal porosities and more favorable fatigue resistance. In lower fatigue life regimes, minimal differences between virgin and recycled fatigue samples were reported and were attributed to similar surface finish after polishing fatigue samples.

Studies like those reviewed above have demonstrated the importance of powder feedstock characteristics – both with careful consideration of the particle size distribution utilized and amount of reuse with respect to laser and build parameters. It is clear that feedstock particle size

distribution should be considered when manufacturing AM parts, as they may play an important role in as-printed part density, microstructure and mechanical properties. As it stands, more research is needed before a rigorous and standardized SLM parametric matrix can be developed. Many of the phenomena that occur within the build chamber, e.g. melt and laser interaction and powder packing factor, are impacted by the powder size and shape. However, the extent of this relationship has been shown to vary significantly across different alloys and SLM systems. In terms of powder recyclability in AM, there appears to be some discrepancies depending on the process and alloy utilized. However, the general consensus among the studies discussed here is that powder recycling is feasible and not necessarily detrimental to mechanical strength and part microstructure. Therefore, in this work, the effects of both particle size distribution and recycling for Al10SiMg in the SLM process were examined after optimization of gas atomization to produce Al10SiMg alloy powder feedstock specifically for this study.

CHAPTER 3: EXPERIMENTAL METHODOLOGY

3.1 Parametric Investigation of Gas Atomization

A double induction, CCGA unit, presented in Figure 5 (designed and manufactured by Dong Yang Induction Melting Furnace Co. Ltd., Republic of Korea) was used for all gas atomization experiments. Figure 6 illustrates a schematic configuration of the gas atomization system and peripheral machinery utilized. The gas atomization process was carried out for the Al10SiMg alloy which has a nominal composition of 10 wt.% Si, 0.5 wt.% Mg (Al bal.). Charge alloys contained minor impurities of Fe and Mn, which were less than 0.1%.

Figure 5. Gas atomization system and peripherals

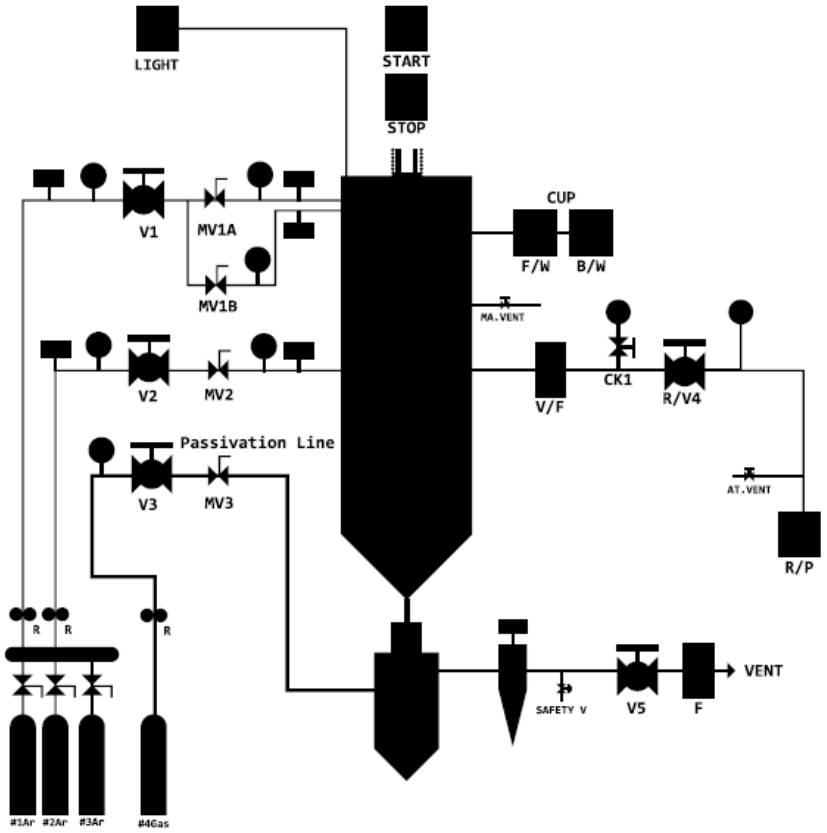

Figure 6. Schematic of gas atomization system

During gas atomization, alloy charge is first placed into a graphite crucible which is housed by an induction furnace. Then, the charge is inductively melted in an open-air environment. The charge temperature can be preset and is typically controlled by manipulating the input power (kW) on the induction heating control panel located on the atomization unit. In this study, the charge temperature range between 850°C and 1000°C was examined. Once the charge is molten, it is poured using a motorized mechanism where the molten liquid alloy flows into the atomization chamber through a holding crucible and orifice, which is held at a preset "orifice temperature." The pouring mechanism and hold crucible assembly is depicted in Figure 7.

Figure 7. Crucible set-up and pouring of molten liquid of metallic alloy

Orifice diameter can be varied and directly affects the melt flow rate. By changing the orifice diameter between 2.0 mm and 3.5 mm, mass flow rate of molten alloy into the atomization chamber varied from 0.013 kg/s to 0.036 kg/s, respectively. The atomization chamber can be evacuated and backfilled with either Nitrogen or Argon gas. However, for the purposes of this study, the chamber was not evacuated or backfilled, i.e., atomization in air environment. A comprehensive matrix containing values for all parametric studies is listed in Table 5.

Table 5. Comprehensive parameter matrix for gas atomization study

Parametric Study Experiments	**Melt Flow Rate (kg/s)**	**Gas Pressure (MPa)**	**Melt Temperature (°C)**
Melt Flow Rate	**0.012 – 0.037**	2.0 ± 0.1	950
Gas Pressure	0.019 ± 0.002	**1.4 – 3.1**	950
Melt Temperature	0.034 ± 0.003	2.1 ± 0.2	**850 – 1000**

Once the molten metal enters the atomization chamber, gas flows are initiated by controls on the vacuum and pressure control unit of the atomizer. Gas tanks are located on the bottom floor of the atomization system and are routed to the inside of the chamber through the V1 valve shown in Figure 6. For the atomization of this alloy, ultra-high purity nitrogen was used as the atomizing gas. The atomizing gas pressure is set with the installed pressure reducing regulators (MV1A, MV1B), and its variation from 1.4 MPa to 3.1 MPa was examined in this study. After initiation of high pressure gas flow, the molten metal is broken-up and rapidly solidified into powders. Powders can then be extracted from the chamber following an adequate amount of cool down time.

Following extraction, metal powders were sieved using industry standard sieves in conjunction with a Ro-Tap® mechanical shaker. The sieve sizes utilized were 212 μm (No. 70), 106 μm (No. 140), 75 μm (No. 200), 63 μm (No. 230), and 45 μm (No. 325). After sieving, particle size of powder samples was measured using particle size analysis (PSA) via Beckman-Coulter Laser Diffraction LS13-320 Particle Size Analyzer. This was carried out to confirm effectiveness of the sieving process and to document the particle size distribution for subsequent AM fabrication. Three different powder yields were defined for this study and measured utilizing digital scale. Quantification for each powder yield (bulk, Y75, Y45) and flow rate of atomization are given by:

$$\text{bulk yield} = \frac{\text{powder yield (g)}}{\text{charge weight (g)}} * 100\% \quad (6)$$

$$\text{Y75} = \frac{\text{powders} < 75\mu\text{m (g)}}{\text{total powder yield (g)}} * 100\% \quad (7)$$

$$\text{Y45} = \frac{\text{powders} < 45\mu\text{m (g)}}{\text{total powder yield (g)}} * 100\% \quad (8)$$

$$\text{flow rate} = \frac{\text{charge weight (kg)}}{\text{duration of atomization (s)}} \quad (9)$$

Bulk yield defined in equation (6) represents the total amount of powder produced from alloy charge melted. Loss of bulk alloy mass is primarily due to slag formation and loss during transient atomization at the start and at the end of the batch run. The Y75 and Y45 yields, according to equations (7) and (8) are defined as "size-specific" yields – and are within the particle size range that can be effectively utilized in PBF AM, more specifically, the SLM process. Molten alloy flow rates were determined utilizing equation (9). This flow rate refers to the duration of atomization for the melt specifically and is not to referring to the gas flow rate.

Comprehensive microstructural characterizations were conducted for as-atomized powders. This characterization includes observation of powder morphology by scanning electron microscopy (Zeiss Ultra-55 SEM), identification of phases and electron energy loss spectroscopy (EELS) via TEM (FEI/Tecnai™ F30 300kV), and observation of powder microstructure via optical microscopy (OM; Olympus LEXT OLS 3000) to obtain measurements necessary to calculate secondary dendrite arm spacings (SDAS) and estimate cooling rates. After metallurgical sample preparation, cross-sectioned powders were etched with Keller's Reagent to reveal microstructure. The microstructure after polishing and etching was observed via OM. Subsequent quantification of particle characteristics (i.e., SDAS, cooling rates) was carried out utilizing measurements obtained from image analysis through open source ImageJ software (National Institutes of Health).

3.2 Fabrication of Samples using SLM

Preceding sample fabrication, metal powders were sieved according to the procedure detailed in section 3.1 Parametric Investigation of Gas Atomization, and characterized for particle size distribution using the laser diffraction PSA technique. An SLM® 125HL (SLM Solutions, Germany) LBPF system pictured in Figure 8 was used to fabricate all Al10SiMg samples. This system is equipped with a single, continuous IPG fiber laser (400W), laser beam focus diameter of 100µm, and spot size of 70µm. The maximum build volume and build rate of the system are 125 cm^3 and 25 cm^3/hr, respectively.

Figure 8. SLM Solutions Selective Laser Melting 125HL unit

A schematic in Figure 9 illustrates the internal configuration of the SLM machine. Powder feedstock is fed into the build chamber through the hopper and spread across the build plate via the recoater. The laser then follows a slice file (generated from a computer aided design) to selectively melt the layers to build the component. The build plate is then lowered, by a distance

of preset “slice thickness” before being passed over by another powder layer. Unused powders are swept into “overflow” bottles located underneath the build chamber. This process is repeated until the entirety of the component is built. For all SLM studies, cubic and tensile specimen were manufactured for analysis. Cubic samples were fabricated with dimensions of 12 x 12 x 12mm. Tensile specimens were built in a horizontal build orientation and had a gauge length of 25mm, following ASTM standards (ASTM E8/E8M). All samples were manufactured within the build chamber with flowing Nitrogen.

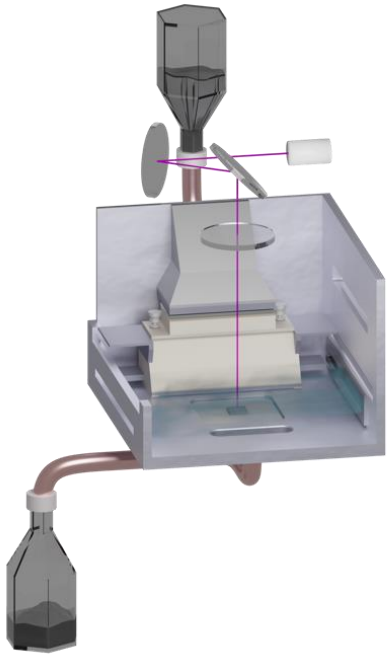

Figure 9. Internal configuration of SLM 125HL build chamber

After fabrication, all samples are removed from the build plate. Cubic samples were measured for relative density using Archimedes’ Principle (ASTM B962). Lateral and bottom sides of cubic samples were grinded down using Si-C grinding pads to smooth the outer surfaces and prevent trapped air bubbles during measurement, which can skew data. Following Archimedes’ experiments, two cross sections were observed for each cubic sample. Cross sections

are designated as; transverse or XY cross section, which is perpendicular to the build direction, and longitudinal or XZ cross section which is parallel to the build direction. These cross sections are illustrated in Figure 10. Metallurgical sample preparation was carried out on cross-sectioned cubic samples according to ASTM standards (ASTM E3) and polished down to 1µm. Samples were then observed under optical microscopy, and image analysis was conducted to obtain area percentages of internal defects such as porosity and lack-of-fusion flaws.

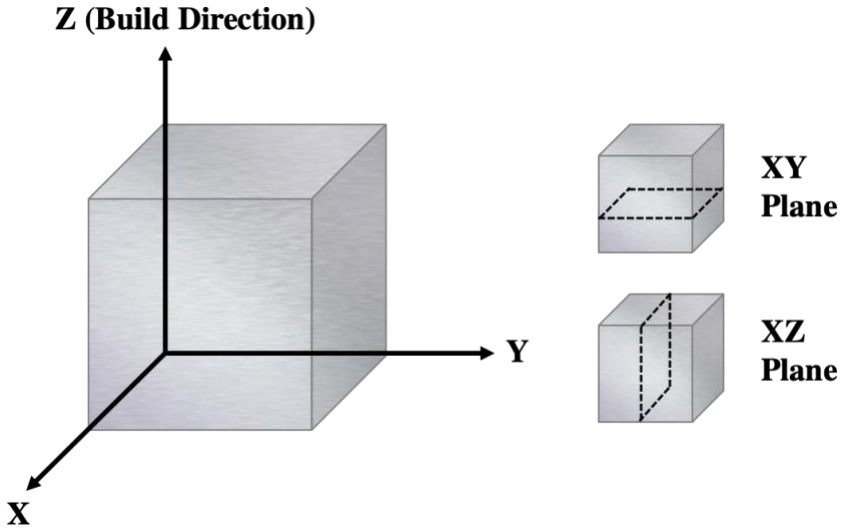

Figure 10. Schematic of cubic sample cross sections used for microstructural analyses

3.2.1 Effects of Particle Size Distribution on SLM Parts

To identify the optimal feedstock particle size distribution for use in SLM, a total of 3 cubic samples and 3 tensile bars (ASTM) were fabricated with Al10SiMg powders for each particle size distribution listed in Table 6. Powder feedstock was first sieved to obtain the desired particle size distributions, and each distribution was confirmed via PSA. Before printing, all powder feedstock morphology was observed and documented through SEM. For this study, a total of 15 cubic

samples and 15 tensile bars were fabricated. A typical arrangement of the specimen on each build plate is presented in Figure 11. SLM samples were then produced in a Nitrogen atmosphere using parameters listed in Table 6. Samples were removed from the build plate and were prepared for analysis using procedure outlined in section 3.2 Fabrication of Samples using SLM. Porosity area percentages were measured from optical images of cross-sectioned cubic samples and plotted as a function of particle size distribution. Mechanical testing of samples included Vickers Hardness measurements of cubic samples and quasi-static tensile testing.

Table 6. SLM parameters and particle size distributions utilized in PSD study

SLM Parameter	**Value**	**Particle Size Distributions**
Laser Power (W)	250	1. $x \leq 45\mu m$ 2. $20\mu m \leq x < 63\mu m$ 3. $x \leq 75\mu m$ 4. $x \leq 106\mu m$ 5. $75\mu m \leq x < 106\mu m$
Laser Scan Speed (mm/s)	1200	
Hatch Spacing (mm)	0.13	
Slice Thickness (mm)	0.03	

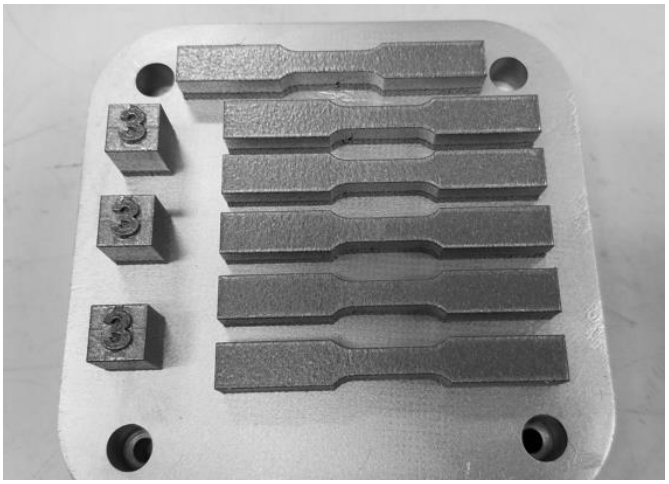

Figure 11. Orientation of samples on build plate for particle size distribution study

3.2.2 Powder Recycling Effects on SLM Parts

The effects of repeated powder reuse in the SLM process was investigated via the following experiments. Cubic and tensile specimen were manufactured utilizing five different powder feedstocks. These feedstocks were reused zero (new or virgin), once, five times, ten times and over twenty times. The particle size range for each powder feedstock was kept constant within the range of 20 – 63 µm, which was achieved by resieving powder feedstock after each use. "Recycled" or "reused" powders in this study were defined as the unused powders collected from the overflow bottles. These powders were not directly melted by the laser but were exposed to laser radiation and heat through conduction in the build plate. Therefore, to standardize the particle size utilized and eliminate any enlarged and agglomerated particles, sieving of powder feedstock with 100µm sieve was conducted after each use.

Microstructural analysis was conducted on both powder feedstock and SLM samples. Each powder feedstock was observed under SEM in order to identify any morphological changes that may have occurred as a result of exposure to the laser in the SLM process. Feedstock powders were then cross sectioned in order to measure particle size and circularity values of powder particles after repeated recycling.

For each powder feedstock, a total of 12 cubic and 3 tensile specimens were produced by SLM. For cubic samples, the parameters tabulated in Table 7 were examined. Three cubes were printed for each parameter set and powder feedstock, resulting in a total of 60 cubes for this study. For all tensile specimen printed in this study, parameter set 1 was utilized. The orientation of samples on the build plate is presented in Figure 12. After the SLM process, defect area percentages were measured from optical images of cross-sectioned cubic samples and plotted

against the number of uses. Microstructural analysis was concluded with measurement of melt pool geometry of cubic samples, i.e., melt pool depth/width. Details regarding this analysis can be found in the following section: 3.3 Microstructural Characterizations and Image Analysis. Mechanical testing included tensile testing of dog-bone samples.

Table 7. Parameter matrix for SLM recycled powder study

Parameter Sets	**Power (W)**	**Hatch Spacing (mm)**	**Scan Speed (mm/s)**	**ED (J/mm^3)**
(1) SLM	350	0.13	1650	54.4
(2) UCF	250	0.13	1200	53.4
(3) High E.D.	250	0.13	600	106.8
(4) Low E.D.	250	0.13	3200	20.0

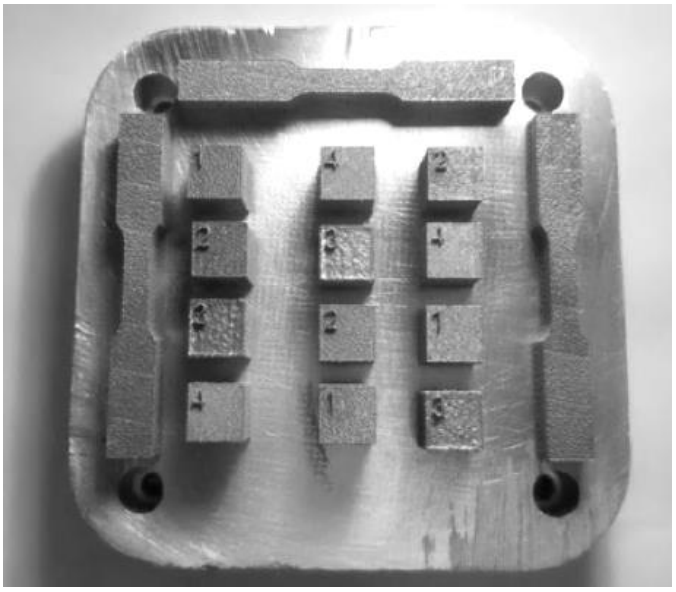

Figure 12. Orientation of samples on build plate for recycled powder study

3.3 Microstructural Characterizations and Image Analysis

Microstructure of powder feedstock, SLM components and porosity of all specimens was examined first by optical microscopy. ImageJ image analysis software was utilized to quantify various factors including dendrite arm spacing, porosity area percentages and melt pool geometry. Microstructure of SLM parts was observed by cross-sectioning cubic samples. For each cubic sample, the XY and XZ cross-sections were polished and observed under OM. Figure 13 illustrates the mounting configuration for cross-sectioned cubic samples.

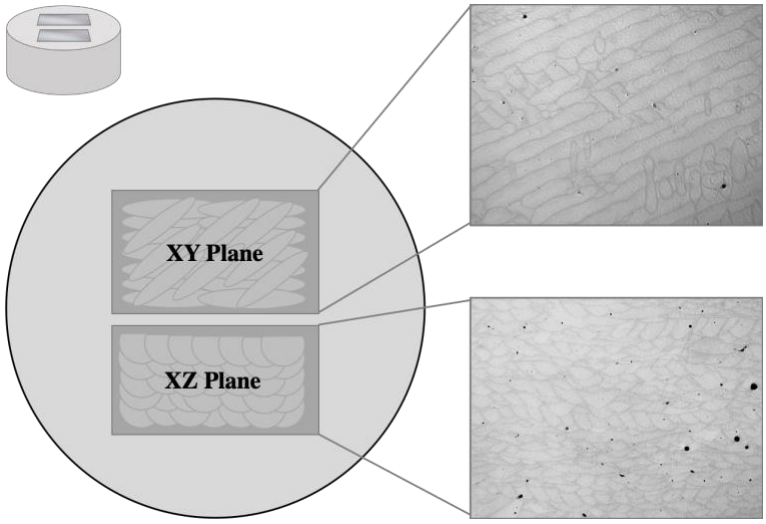

Figure 13. Schematic of mounting configuration for cross-sectioned cubic SLM samples

For each cross section, five micrographs were obtained, resulting in ten micrographs for each cubic sample. Each micrograph was imported into ImageJ and was used to quantify porosities, as an area percentage, and porosity circularity. Circularity values are determined using aspect ratios and are designated by a numerical value from 0 – 1, where a value of 1 indicates a perfectly circular porosity. Figure 14 depicts an example of image thresholding and analysis conducted in ImageJ.

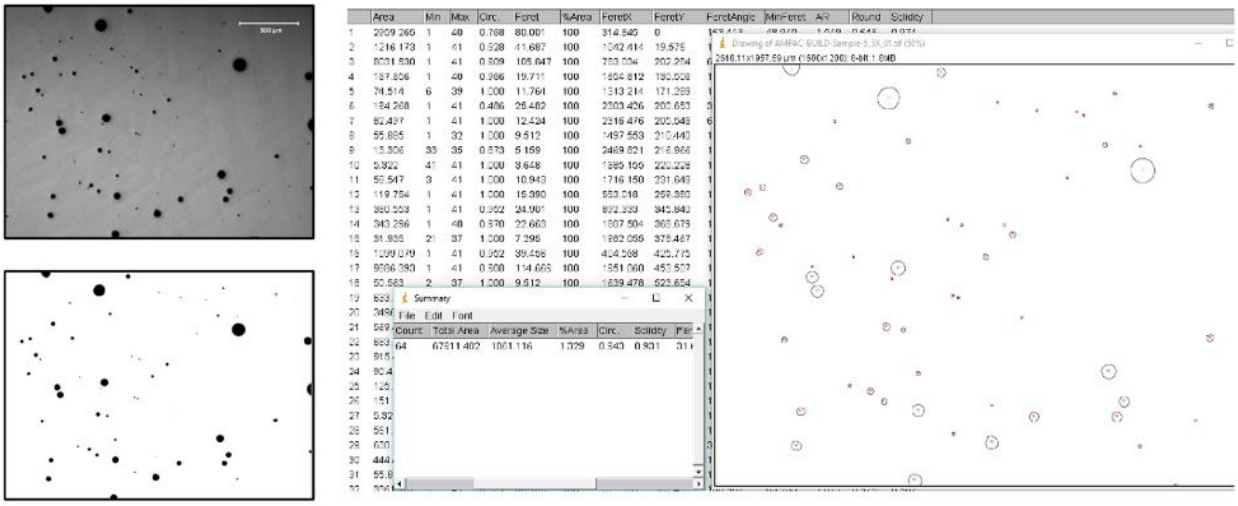

Figure 14. Image thresholding and microstructural measurements in ImageJ

3.4 Mechanical Testing of Samples

The mechanical testing of the Al10SiMg alloy samples included measurements of Vickers Hardness and determination of tensile properties. The hardness of cubic samples was measured with a Vickers hardness tester (Leco™ LV700) with load of 10 kgf and dwell time of 10 seconds. For each cube sample, a total of 15 Vickers hardness measurements were obtained. Tensile bars were printed in a horizontal build orientation and had gauge length of 25mm, following ASTM standards (ASTM E8/E8M). These tensile samples were used to perform quasi-static uniaxial tensile tests with an MTS universal testing machine. During tensile testing, deformations were recorded and measured using the Digital Image Correlation (DIC) technique. A DIC camera placed perpendicular to the loading direction with frequency of 1 Hz was used for all testing. Engineering stress and strain curves were obtained from the MTS machine with a virtual extensometer.

CHAPTER 4: RESULTS

4.1 Gas Atomization Parametric Study

Parametric investigations of the gas atomization process included experiments to determine the effects of melt flow rate, atomizing gas pressure and melt temperature on total and per-particle-size powder yields. Microstructural characterizations by using OM, SEM and TEM were carried out for as-atomized powders. Image analysis of powder microstructure allowed for the calculation of SDAS and estimation of cooling rates for as-atomized Al10SiMg.

4.1.1 Effect of Melt Flow Rate

Melt flow rate was hypothesized to be the most influential parameter involved in gas atomization. In order to identify correlations between melt flow rate and as-atomized powder characteristics, it was first necessary to identify a methodology for controlling melt flow rate. This was achieved by conducting a total of sixteen gas atomization experiments with varying orifice diameter. These experiments included variation of the orifice diameter in the following increments: 2.0 mm, 2.5 mm, 3.0 mm, and 3.5 mm and were carried out at a fixed melt temperature of 950°C and a gas pressure of 2.0 MPa. Averaged results from these atomization runs are listed in Table 8.

Table 8. Relationship between orifice diameter and flow rate

Orifice Diameter (mm)	Number of Runs	Flow Rate (kg/s)
2.0	4	0.013 ± 0.001
2.5	4	0.016 ± 0.002
3.0	4	0.024 ± 0.003
3.5	4	0.036 ± 0.002

Data from orifice diameter experiments are plotted in Figure 15. Results supported the hypothesis that increasing orifice diameters would correlate to increasing melt flow rates. All following gas atomization runs were conducted using the preset orifice diameters listed in Table 8 to achieve the approximate desired melt flow rate.

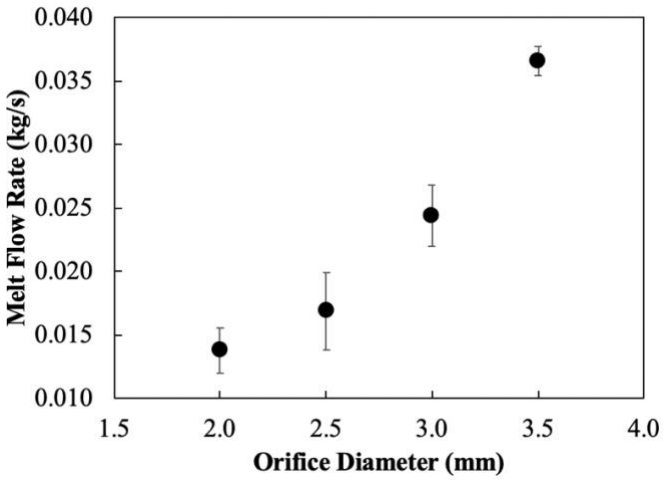

Figure 15. Relationship between orifice diameter and melt flow rate

Figure 16 presents the per-particle-size yield data for gas atomization runs conducted with controlled melt flow rates. Four gas atomization runs were conducted with atomizing gas pressure of 2.0 MPa and melt and orifice temperatures of 950°C and 850°C, respectively. Per-particle-size powder yield is presented as a weight percentage respective to the gross yield of atomized powder for each run. In these experiments, the range of melt flow rates studied was 0.0134 kg/s to 0.0354 kg/s. At lower melt flow rates, powder yield is shifted towards smaller size distributions, with the highest yields occurring for powders less than 45 µm. At higher melt flow rates, powder yields are greatest for larger particle size distributions. For applications in SLM, powders within the range of 75 µm or less are typically used [16]. Therefore additional atomization runs were conducted to

confirm the trend observed in Figure 16, with respect to yield for powders in this range, namely Y75 and Y45 yields, which were defined in section 3.1 Parametric Investigation of Gas Atomization of this thesis.

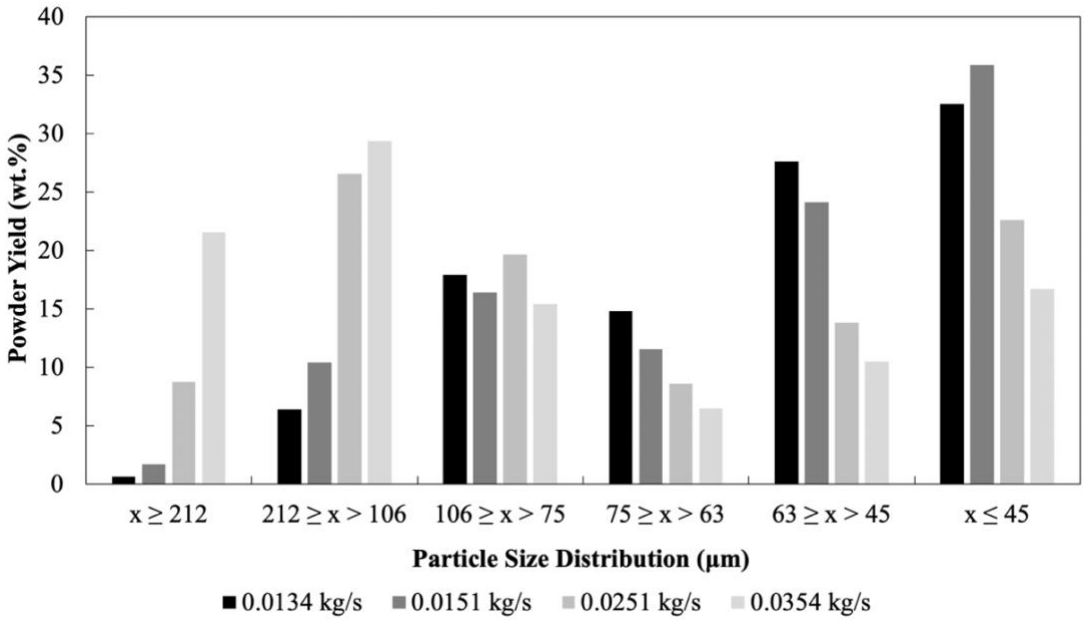

Figure 16. Effects of melt flow rate on per-particle-size distribution

Data listing Y75 and Y45 yields for runs conducted using various flow rates is reported in Table 9. With constant melt temperature and gas pressure, it is clear that increasing melt flow rates leads to decreases in Y75 and Y45 powders. This trend can be observed in Figure 17.

Table 9. Y75 and Y45 powder yields at various melt flow rates

Flow Rate (kg/s)	**Y75 (wt.%)**	**Y45 (wt.%)**
0.014 ± 0.001	72.8 ± 2.0	34.1 ± 1.5
0.017 ± 0.002	63.8 ± 4.2	31.7 ± 2.7
0.024 ± 0.003	52.0 ± 4.7	24.9 ± 2.0
0.036 ± 0.002	34.1 ± 0.6	17.6 ± 1.3

Highest Y75 and Y45 yields were achieved when atomizing with a melt flow rate of 0.014 ± 0.001 kg/s, which corresponds to the use of 2.0 mm orifice diameter. Contrarily, the lowest yields were observed after atomizing with a melt flow rate of 0.036 ± 0.002 kg/s. Over the range of melt flow rates utilized, Y75 and Y45 powder yields consistently decreased with increasing flow rates. Results confirm the trend observed in Figure 16 and suggest an inverse relationship between melt flow rate and yield for finer powders.

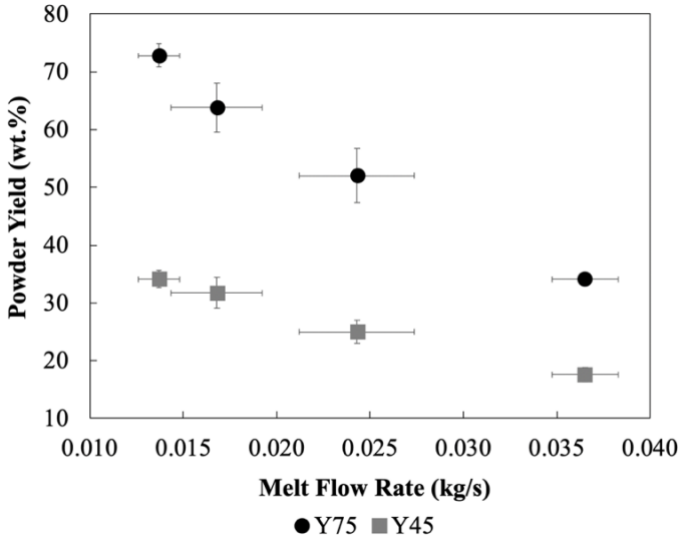

Figure 17. Y75 and Y45 yields as a function of melt flow rate

4.1.2 Effect of Atomizing Gas Pressure

In order to identify the relationship between gas pressure and powder yield, gas atomization was conducted using a range of pressures from 1.4 MPa – 3.1 MPa. Atomization proceeded successfully at all gas pressures investigated. Data from twelve atomization experiments was analyzed to identify the relationship between gas pressure and yield for finer powders. Averaged data from these runs are listed in Table 10 and plotted in Figure 18. All atomization runs for

pressure analysis were conducted with melt flow rate of 0.0195 ± 0.002 kg/s and melt and orifice temperatures of 950°C and 850°C, respectively.

Table 10. Y75 and Y45 powder yield values at various atomizing gas pressures

Gas Pressure (MPa)	Y75 (wt.%)	Y45 (wt.%)
1.4 ± 0.17	58.16 ± 5.77	30.22 ± 2.36
2.0 ± 0.00	65.94 ± 8.31	35.49 ± 5.97
2.7 ± 0.16	80.76 ± 4.70	41.91 ± 2.64
3.1 ± 0.12	77.68 ± 7.29	40.76 ± 2.76

For the first three pressure values, slight increases in both Y75 and Y45 powder yields were observed. However, at 3.1 ± 0.12 MPa, the highest gas pressure examined for this study, powder yields were slightly less. From these experiments, atomization parameter set with gas pressure of 2.7 ± 0.16 MPa, melt flow rate of 0.0195 ± 0.002 kg/s, and melt temperature of 950°C resulted in the highest Y75 yield of 80.76 ± 4.70 wt.%.

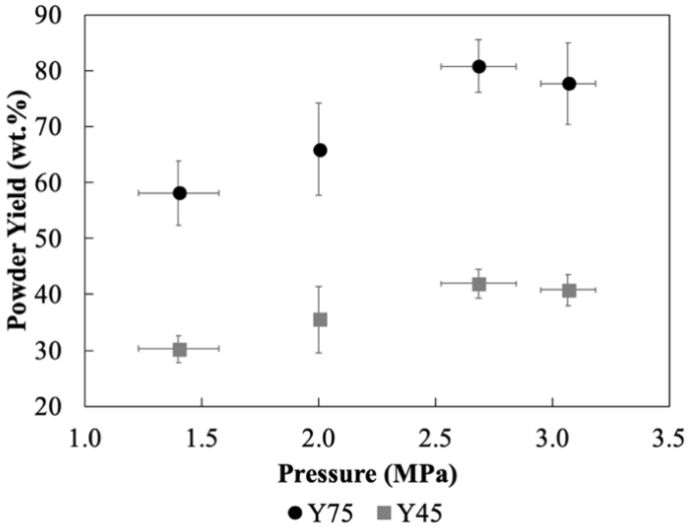

Figure 18. Y75 and Y45 powder yield as a function of atomizing gas pressure

4.1.3 Effect of Melt Temperature

To identify the effects of melt temperature on Y75 and Y45 powder yields, gas atomization data from twelve runs was analyzed. Each atomization run was conducted with melt flow rate of 0.034 ± 0.003 kg/s and gas pressure of 2.04 ± 0.009 MPa. Melt and superheat temperatures utilized in experiments are listed in Table 11 along with corresponding Y75 and Y45 powder yields. Superheat is the temperature in Kelvin above the melt temperature of the Al10SiMg alloy at 570°C.

Table 11. Y75 and Y45 powder yield values at various melt and superheat temperatures

Melt Temperature (°C)	**Superheat (K)**	**Y75 (wt.%)**	**Y45 (wt.%)**
850	280	40.83 ± 8.1	20.94 ± 5.9
900	330	41.29 ± 8.2	22.39 ± 7.5
950	380	43.29 ± 4.5	23.48 ± 4.5
1000	430	37.18 ± 1.4	18.48 ± 0.8

Trends similar to those of the gas pressure analysis were observed for the various melt temperature runs. The lowest Y75 and Y45 powder yields were observed when atomizing with melt temperatures of 850°C. Combined melt temperature of 950°C, melt flow rate of 0.034 ± 0.003 kg/s, and gas pressure of 2.04 ± 0.009 MPa resulted in the highest Y75 yield of 43.29 ± 4.5 wt.%. Again, trends indicate slight increases in powder yield, however within the uncertainty, for the first three temperatures utilized. At 1000°C, the highest temperature utilized for this study, Y75 and Y45 yields were less than those using melt temperatures of 850°C – 950°C.

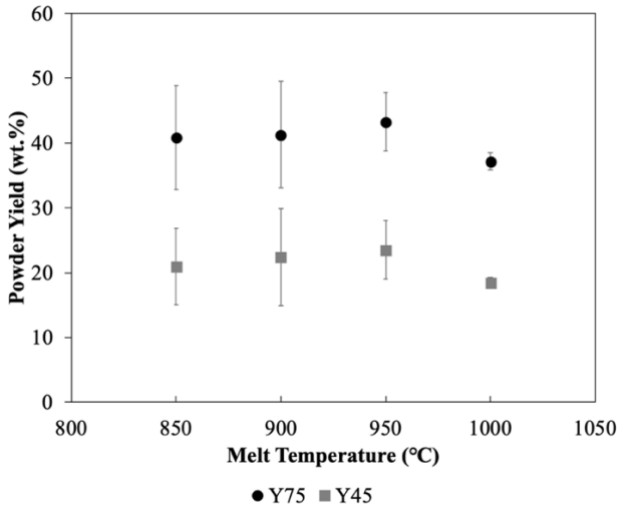

Figure 19. Y75 and Y45 powder yields as a function of melt temperature

4.1.4 Quantification of Porosities in As-Atomized Powders

A typical optical micrograph from cross-sectioned Al10SiMg powders is shown in Figure 20. Porosity area percentages for each particle size distribution were obtained from a minimum of one hundred powder particles for each particle size distribution. Porosity data is presented in Table 12 and graphed in Figure 21. While porosity in powders are not overall significant, results demonstrate a clear decreasing trend for porosity with respect to decreasing particle size.

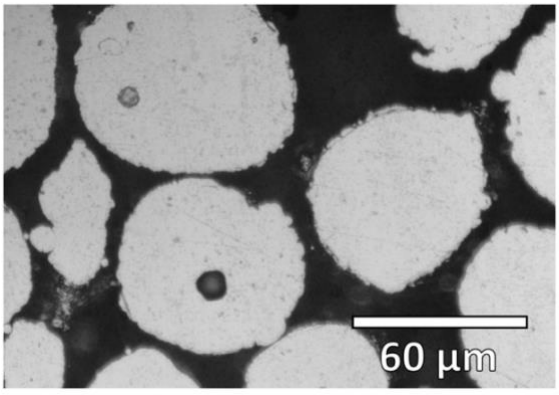

Figure 20. Example optical micrograph of cross sectioned Al10SiMg powders used for porosity measurements

Table 12. Tabulated porosity area percentages for cross sectioned Al10SiMg powder

Particle Size Distribution (µm)	Porosity Area (%)
$212 \geq x > 106$	1.047 ± 0.24
$106 \geq x > 75$	0.392 ± 0.13
$75 \geq x > 63$	0.207 ± 0.05
$63 \geq x > 45$	0.203 ± 0.08
$x \leq 45$	0.069 ± 0.07

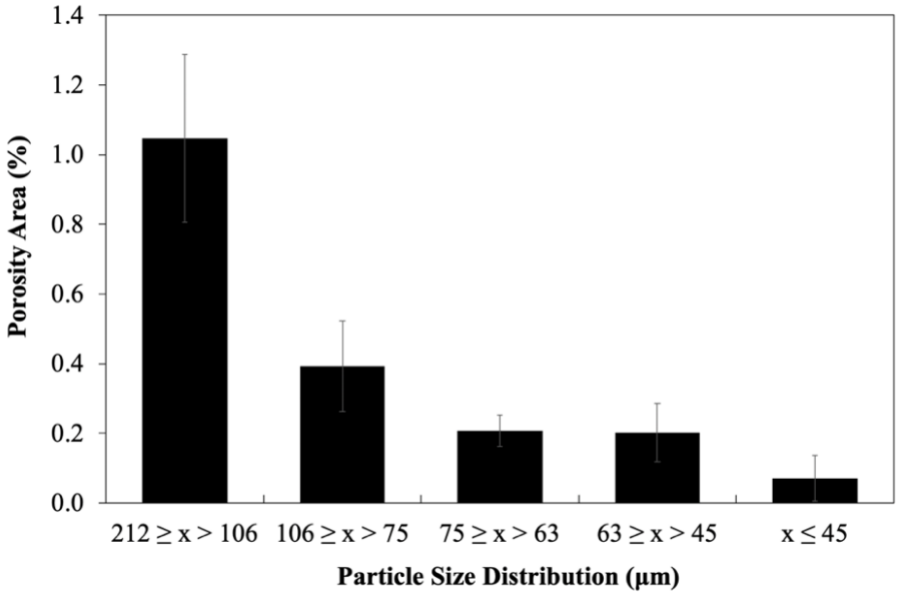

Figure 21. Porosity area percentages for cross sectioned Al10SiMg powders

4.1.5 Microstructural Analysis of Atomized Powders

Typical as-atomized powder morphology for Al10SiMg was observed via SEM and is presented in Figure 22. Powders appear mostly spherical with the presence of small "satellites" on the surface of powder particles. Al10SiMg powders were then cross sectioned and etched with Keller's reagent and examined using OM. A representative Al10SiMg particle is shown in Figure

23. Formation of dendrites is shown clearly, and microstructure exhibits primary α-Al and interdendritic eutectic region.

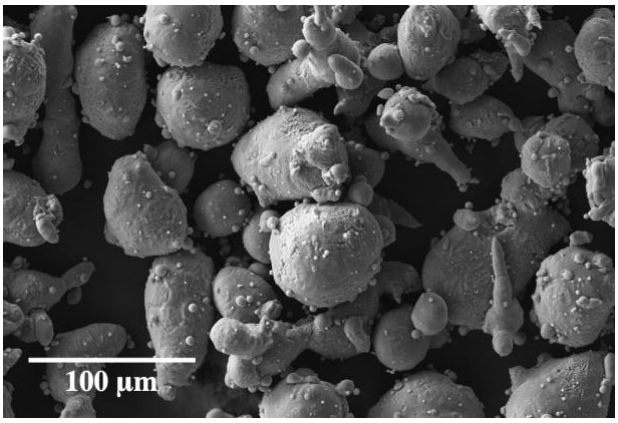

Figure 22. Morphology of Al10SiMg observed under SEM

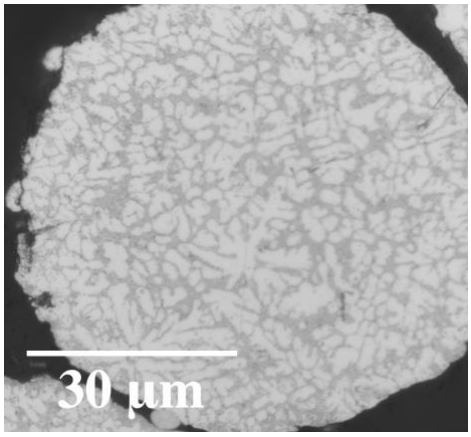

Figure 23. Optical micrograph of cross-sectioned Al10SiMg powders

Detailed microstructural features of Al10SiMg alloy were examined via TEM. Figure 24(a) shows the primary α-Al phase and lamellar eutectic structure (α-Al+Si) in the SLM microstructure. Figure 24(b) presents discrete selected area diffraction pattern (SADP) from lamellar Al and Si, observed by the selected area diffraction pattern (SADP) obtained from Al10SiMg powders. Oxide scale that covers the atomized powders is shown in Figure 24(c) with the bright-field TEM

micrograph. Results from EELS analysis are shown in Figure 24(d) and Figure 24(e), and confirmed the presence of oxide scale covering powders, with approximate thickness of 10 nm.

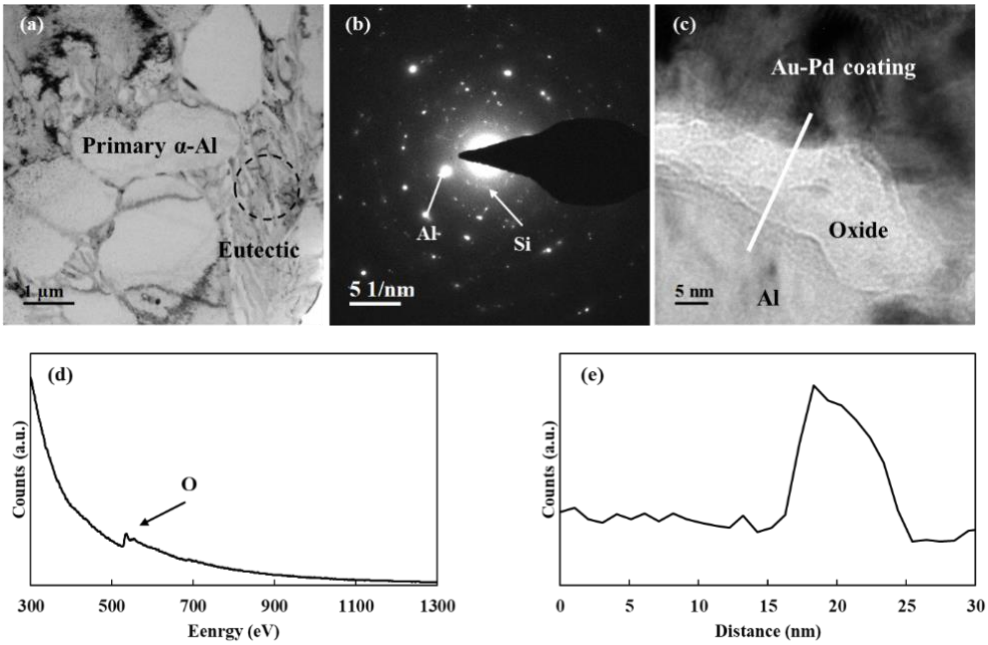

Figure 24. TEM analysis of Al10SiMg (a) cell and eutectic structure of as-built SLM sample (b) SADP from eutectic structure of powders (c) micrograph of oxide layer (d) EELS spectrograph depicting the O peak, (e) counts of the O peak from the EELS scan

4.1.6 SDAS and Estimated Cooling Rate for Al10SiMg Powders

Micrographs of cross-sectioned powders, as presented in Figure 23 were used to measure particle diameters for over eighty Al10SiMg particles. Relationship between SDAS and particle size for gas atomized Al10SiMg is given by Eq. (10) where the $D_{particle}$ is the particle diameter [50]. Coefficient and exponent values in this equation are material and process dependent [51]. SDAS are known to vary with respect to particle size and can be related to cooling rates. However, cooling rate calculations from SDAS typically require extensive efforts to determine coarsening behavior and theoretically calculated cooling curves, which are material specific [52]. Therefore,

in this thesis, SDAS calculations will be related to particle size and powder cooling rates will be estimated via a simplified model based on convection heat transfer principles.

$$SDAS = (0.14 \cdot D_{particle})^{0.61} \quad (10)$$

Using this relation and particle size measurements, the trend in Figure 25 was obtained. SDAS were observed to increase for increasing particle size. Particles with diameters of 4.3 µm and 146 µm gave SDAS values in the range of 0.74 µm to 6.3 µm.

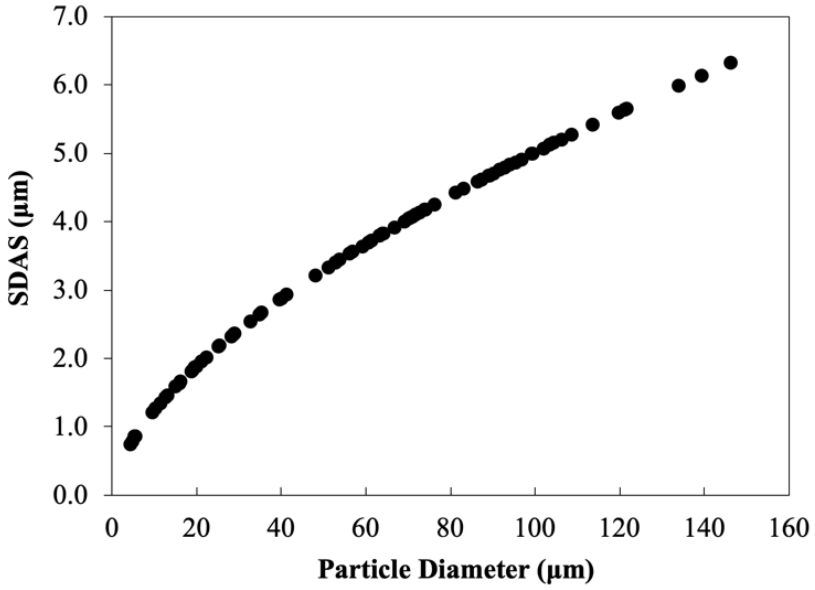

Figure 25. Calculated secondary dendrite arm spacings for Al10SiMg gas atomized powders as a function of particle diameter

Shiwen *et* al. [53] proposed a simple theoretical model for calculating the cooling rates of gas atomized powders. This model was developed based on convection heat transfer principle and was derived by applying a heat balance condition to the molten droplets in atomization during solidification within the ambient environment of the atomization chamber. Heat transfer coefficient between inert gas and molten droplets, formation of spherical droplets and assumed

zero relative velocity between droplets and atomizing gas were all taken into account for this model which can be simplified according to Eq. (11). Values k_g, ρ, C_p, d, T_d and T_f are thermal conductivity of atomizing gas, density and specific heat of material, droplet size, droplet temperature and gas temperature, respectively.

$$\left| \frac{dT_d}{dt} \right| = \frac{12 \cdot k_g}{\rho \cdot C_p \cdot d^2} \cdot (T_d - T_f) \qquad (11)$$

Thermophysical properties specific to the Al10SiMg alloy and Nitrogen gas are listed in Table 13. Density [54] and specific heat [55] of Al10SiMg were taken from material data sheets and ASTM standards. Thermal conductivity of Nitrogen was taken for temperature of 298 K and 0.1 MPa [56]. For application of this model, several assumptions were made. These assumptions are listed as follows: (1) value of droplet size was taken to be the measured particle size of atomized powders, (2) droplet temperature was taken to be the temperature of molten metal, i.e. melt temperature utilized for atomization, and (3) atomization gas temperature was taken to be ambient temperature. These assumptions were employed for simplicity and were similar to assumptions made by researchers who proposed the model [53].

Table 13. Thermophysical properties of Al10SiMg and Nitrogen gas for convection heat transfer model used to estimate cooling rates for powder

Thermophysical Property	**Value**
Density of Al10SiMg (kg/m^3)	2670
Specific Heat of Al10SiMg (J/kg • K)	910
Droplet Temperature (K)	1223.15
Atomization Gas Temperature (K)	298
Gas Thermal Conductivity (W/m • K)	0.0258

Estimated cooling rates were plotted as a function of particle diameter. This relationship is depicted in Figure 26. Particles with diameter from 4.3 μm to 146.3 μm had estimated cooling rates in the range of 6.3×10^{6} K/s to 5.5×10^{3} K/s, respectively. These cooling rate values are within the range commonly reported for aluminum powders [57, 58] and demonstrate the inverse relationship between cooling rates and particle diameter for the gas atomization process. Limitations of this theoretical model, and suggestions for more precise cooling rate calculations will be discussed in following chapters.

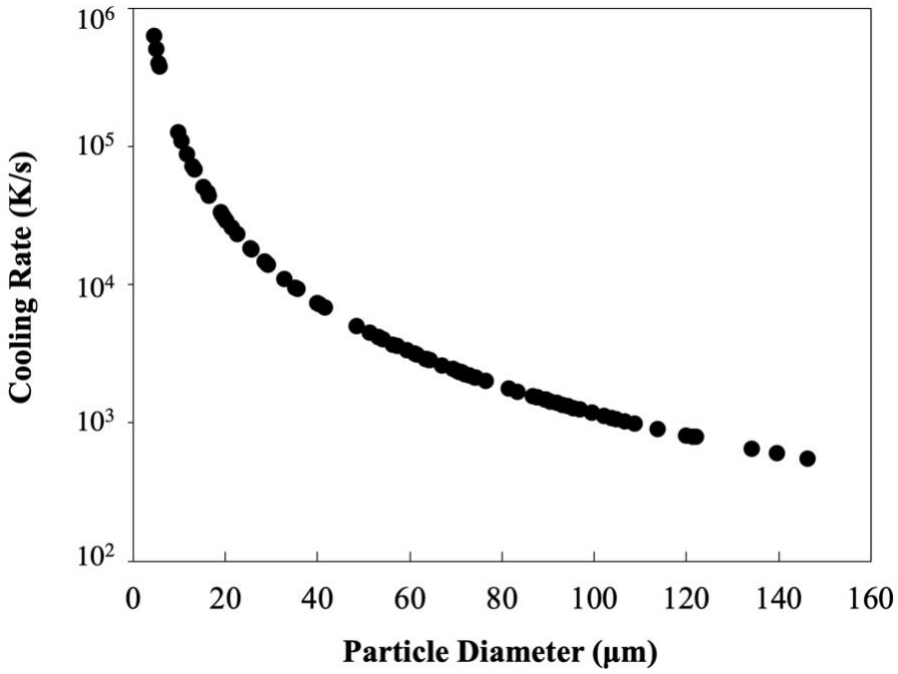

Figure 26. Estimated cooling rates for Al10SiMg as a function of particle diameter calculated using convection heat transfer model

4.2 SLM Particle Size Distribution Study

Particle size analysis was conducted to confirm that powder feedstock for SLM had mean particle size within the range of the distribution selected for study. Results of particle size analysis are listed in Table 14. Values denoted by d10, d50, and d90 are common metrics in particle size analysis and represent the cumulative percentage of powders, i.e., 10%, 50%, 90%, in the sample that fall below that value. For example, a d10 value of 20.8 µm indicates that 10% of the particles in the powder sample have mean particle size smaller than 20.8 µm. By this definition, d50 values should be similar to mean particle size values. In the following sections, each particle size distribution will be identified by its mean particle size, i.e., $x \leq 45$ µm will be labeled as 33.03 µm.

Table 14. Particle size analysis data for each powder size distribution

Particle Size Distribution (µm)	**Mean Particle Size (µm)**	**d10 (µm)**	**d50 (µm)**	**d90 (µm)**
$x \leq 45$µm	33.03	20.8	32.0	47.1
$20\text{µm} \leq x < 63\text{µm}$	42.28	23.6	40.1	64.2
$x \leq 75$µm	44.19	23.5	42.3	67.7
$x \leq 106$µm	68.98	25.7	66.4	114.5
$75\text{µm} \leq x < 106\text{µm}$	92.80	62.8	89.6	131.1

4.2.1 Powder Morphology of each Particle Size Distribution

Morphology of Al10SiMg powder samples is depicted for each particle size distribution in Figure 27. Satellites are observed in all powder samples. From observation of powder morphology, irregular particles seem to be more prevalent for larger mean particle size samples. Conversely, the largest amount of spherical powders was observed in the 33.03 µm powder sample.

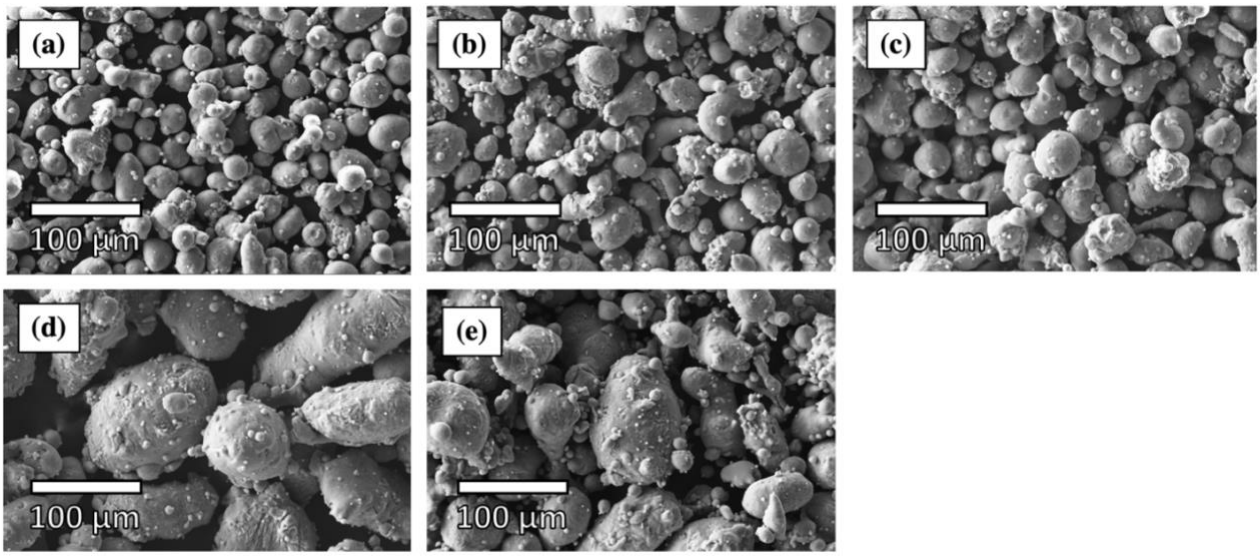

Figure 27. Scanning electron micrographs of Al10SiMg powders with mean particle size (a) 33.03 µm, (b) 42.28 µm, (c) 44.19 µm, (d) 68.98 µm, and (e) 92.80 µm

4.2.2 Effects of Particle Size on SLM Microstructure

An optimized SLM parameter set for the Al10SiMg alloy provided by SLM Solutions was utilized for the fabrication of cubic samples. These parameters are detailed in Table 6 located in the Experimental Methodology chapter. Relative density of these cubic samples was calculated using Archimedes' principle for each mean particle size and are listed in Table 15. Relative densities of 99% were achieved for all powder feedstock utilized.

Table 15. Relative density values for SLM components printed with variable particle size distributions obtained by Archimedes' principle experiments

Mean Particle Size (µm)	Relative Density (%)
33.03	99.51 ± 0.04
42.28	99.49 ± 0.15
44.19	99.93 ± 0.41
68.98	99.82 ± 0.25
92.80	99.70 ± 0.65

Transverse (XY) and longitudinal (XZ) cross sections of cubic samples were observed via OM and used to quantify porosities in as-built cubic samples. Figure 28 presents representative microstructure for each of these cross sections. Minimal porosities without any solidification cracks were observed in all cross sections, with the largest amount of porosities seen in 68.98 µm and 92.80 µm samples. Results from image analysis of samples are listed in Table 16 and depicted graphically in Figure 29.

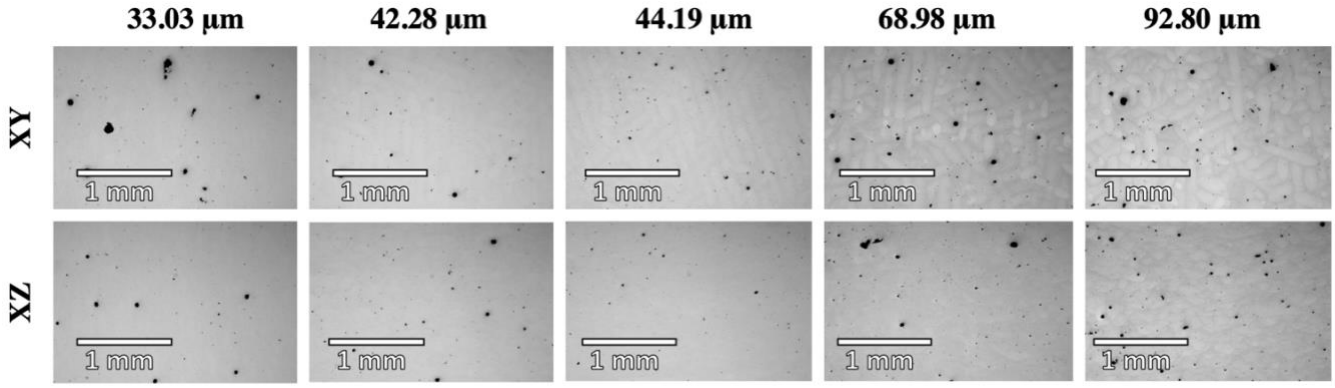

Figure 28. Optical micrographs from the XY and XZ cross-sections of the as-built Al10SiMg alloys using various powder feedstock particle size distributions

Table 16. Porosity area percentages for XY and XZ cross sections obtained via image analysis

Mean Particle Size (µm)	XY Porosity (%)	XZ Porosity (%)
33.03	0.27 ± 0.09	0.32 ± 0.04
42.28	0.25 ± 0.02	0.29 ± 0.02
44.19	0.27 ± 0.03	0.30 ± 0.01
68.98	0.57 ± 0.12	0.59 ± 0.04
92.80	0.54 ± 0.03	0.64 ± 0.04

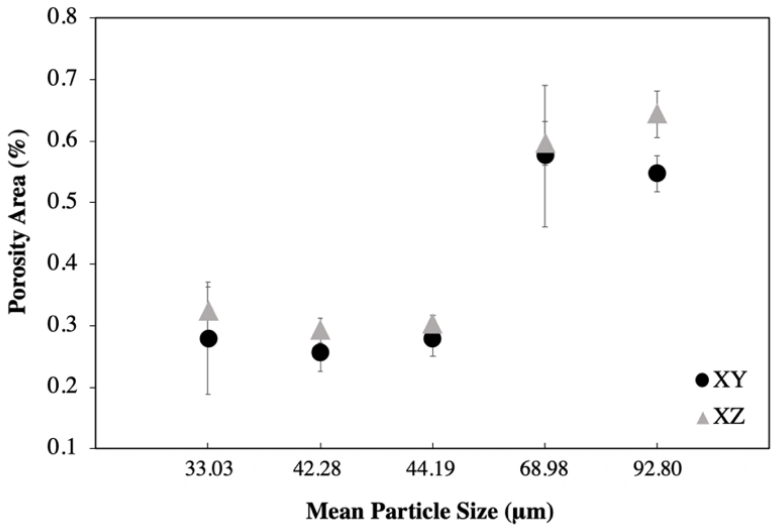

Figure 29. Porosity area percentages of Al10SiMg samples as a function of mean particle size

4.2.3 Effects of Particle Size on Mechanical Properties of SLM Parts

Mechanical testing conducted for the particle size distribution study included Vickers hardness and uniaxial tensile testing. Results from Vickers hardness testing of both the XY and XZ cross sections is presented in Table 17 and Figure 30. While variation in VH values were overall insignificant, the largest values were observed for samples built with 68.98 µm powders.

Table 17. Vickers hardness values for Al10SiMg components printed using feedstock with varying mean particle size for both XY and XZ cross sections

Mean Particle Size (µm)	**Vickers Hardness (XY)**	**Vickers Hardness (XZ)**
33.03	119.9 ± 2.7	119.9 ± 4.4
42.28	119.9 ± 1.8	117.0 ± 1.3
44.19	120.7 ± 1.9	116.9 ± 1.1
68.98	125.3 ± 2.3	122.9 ± 1.6
92.80	124.7 ± 2.9	122.0 ± 2.7

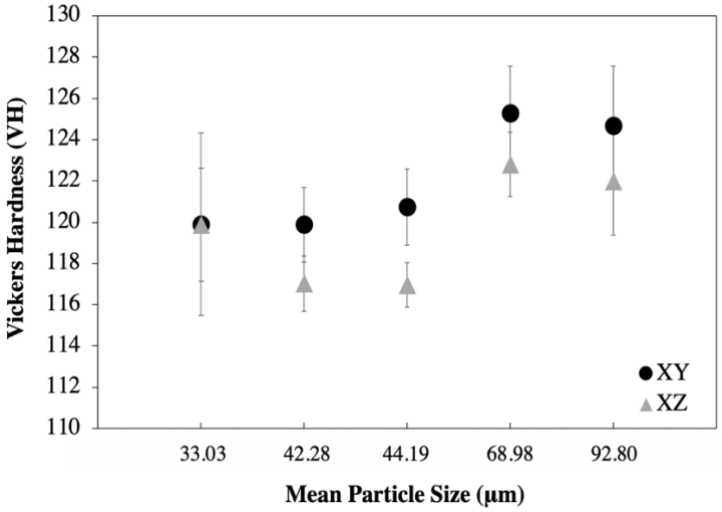

Figure 30. Vickers Hardness of Al10SiMg as a function of mean particle size of feedstock.

Results from tensile testing are listed in Table 18 with standard deviations. Engineering stress strain curves are presented in Figure 31. Largest yield strength (YS) and ultimate tensile strength (UTS) values were 265.1 ± 7.5 MPa and 448.5 ± 5.8 MPa, respectively, and were achieved using powder feedstock with mean particle size of 92.80 µm. Conversely, the lowest YS and UTS values were observed for tensile specimen built with powders with mean particle size of 33.03 µm. Ductility was highest for the specimen produced with mean particle size of 42.28 µm.

Table 18. Room temperature tensile properties with standard deviations for Al10SiMg SLM samples fabricated with various powder feedstock size distributions

Mean Particle Size (µm)	Yield Strength (MPa)	UTS (MPa)	Strain at Fracture	Modulus of Toughness
33.03	228.5 ± 6.4	434.3 ± 3.3	0.090 ± 0.006	32.76 ± 2.49
42.28	241.8 ± 5.3	439.4 ± 1.9	0.096 ± 0.001	36.35 ± 0.53
44.19	247.1 ± 6.8	439.9 ± 0.8	0.094 ± 0.000	35.52 ± 0.24
68.98	254.5 ± 7.1	447.7 ± 4.3	0.085 ± 0.018	32.17 ± 8.01
92.80	265.1 ± 7.5	448.5 ± 5.8	0.070 ± 0.006	25.90 ± 2.89

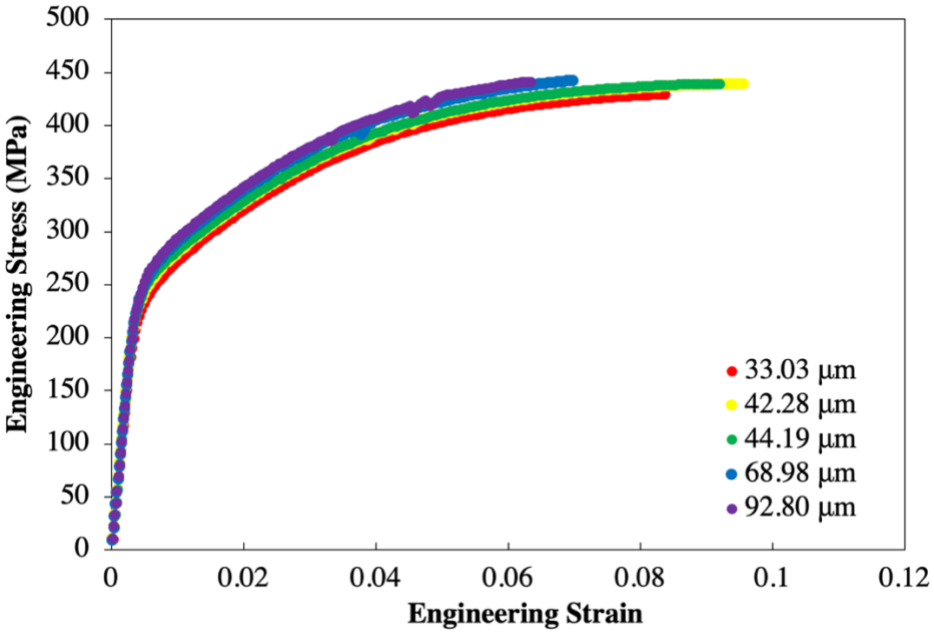

Figure 31. Engineering stress-strain curves of the Al10SiMg alloy in the as-built state for each average particle size

4.3 SLM Recycled Powder Study

To address the concerns of sustainability and economic impacts of SLM, a recycled powder study was conducted. Various feedstock from virgin powder to powders reused over twenty times was utilized. Virgin powder particle size ranged from 20 – 63 µm. Powder characteristics like particle size and circularity were determined after continued reuse. Microstructure and mechanical properties of SLM samples were also analyzed with respect to continued feedstock reuse.

4.3.1 Average Particle Size after Recycling

Following each build, samples of powder feedstock were collected from the build platform and overflow bottles. These samples contained both recycled and dark, slightly vaporized powders which are known as condensate powders [59]. Particle size was measured via image analysis for

each sample preceding sieving. Cross sectioned powder samples for virgin and highly recycled feedstock are depicted in Figure 32. These micrographs illustrate a clear and significant increase in particle size. Additionally, increases in particle irregularity are observed after continuous recycling. To quantify these factors, image analysis was conducted for all recycled powder feedstock. Data from particle measurements is presented in Table 19 and graphed in Figure 33. Results indicate a clear increase in particle size due to coalescence after continued reuse and emphasize the importance of resieving powders between each use. Therefore, before reuse in the SLM process, all powder feedstock was sieved using a 100 µm sieve to eliminate the presence of condensate powders and maintain similar size fractions when printing.

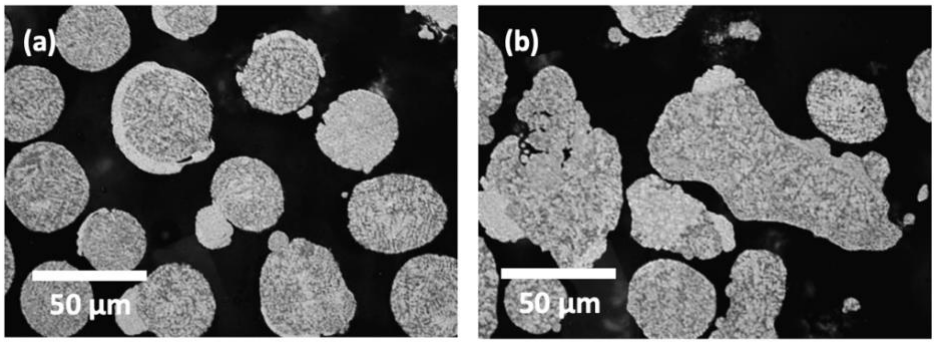

Figure 32. Cross-sectioned Al10SiMg powders after a) zero and b) over twenty reuses

Table 19. Average particle size for Al10SiMg powder feedstock after each use obtained via OM and image analysis

Powder Sample	**Particle Size (µm)**
Virgin	42.5 ± 29.5
Used Once	61.9 ± 30.8
Used Five Times	62.2 ± 39.6
Used Ten Times	76.4 ± 42.9
Used 20+ Times	84.2 ± 81.2

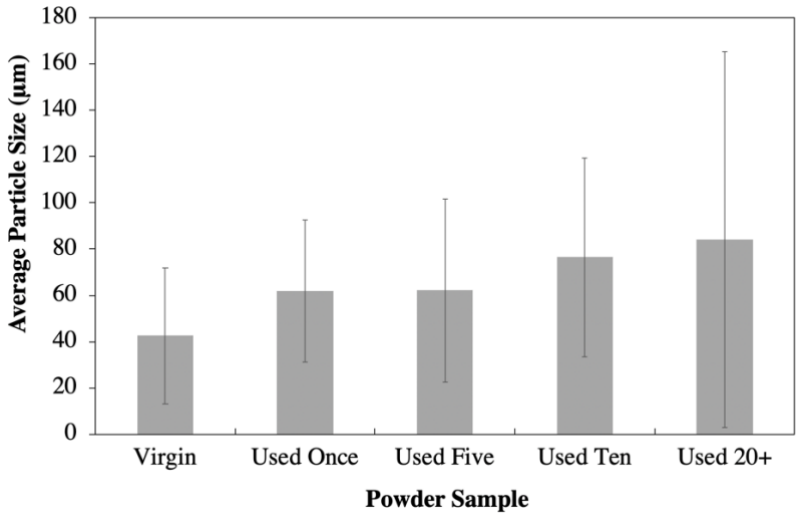

Figure 33. Average particle sizes of various reused Al10SiMg powder feedstock

4.3.2 Powder Morphology after Recycling

Powder morphology for each powder sample after sieving is depicted in Figure 34. Virgin powders appear to be the most spherical with only minimal irregularity observed. Other powder samples exhibit a greater mixture of irregular and spherical particles. Most notably, surface roughness and irregularly shaped particles appear to increase after continued reuse.

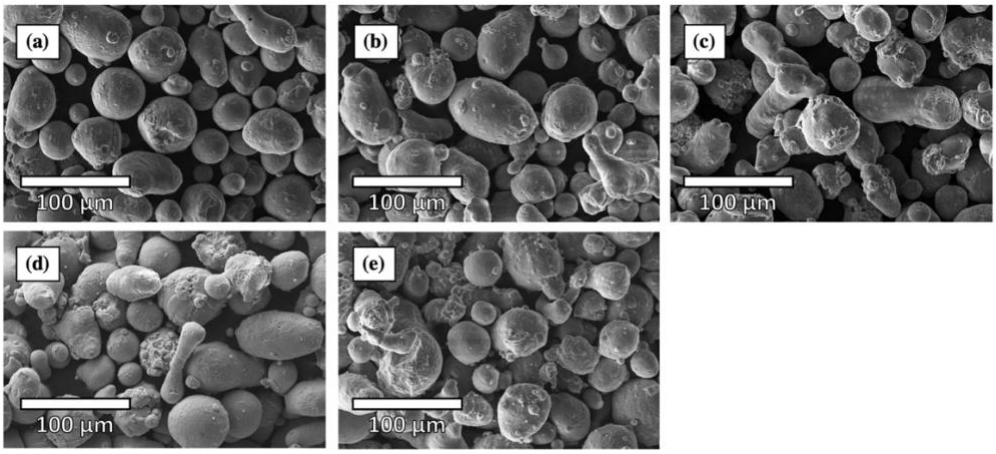

Figure 34. SEM micrographs of Al10SiMg powder morphology after each use (a) virgin, (b) used once, (c) used five times, (d) used ten times, (e) used more than 20 times

4.3.3 Particle Circularity of Powder Feedstock after Recycling

To further clarify observations made from powder morphology, image analysis was conducted to measure the circularity of cross-sectioned powder feedstock after reuse. Circularity values were measured for an average of 708 particles for each powder sample and are listed in Table 20. Values are plotted in Figure 35. Highest circularity value, 0.808 ± 0.013, was obtained from virgin powder samples, and the lowest circularity value, 0.745 ± 0.019, was observed for five times reused powders. Circularity values appeared to decrease continually from 0.808 to 0.745, until after ten and over twenty uses, where the circularity remained unchanged.

Table 20. Circularity values for Al10SiMg powder after each use

Powder Sample	Circularity Value
Virgin	0.808 ± 0.013
Used Once	0.778 ± 0.010
Used Five Times	0.745 ± 0.019
Used Ten Times	0.782 ± 0.017
Used 20+ Times	0.785 ± 0.016

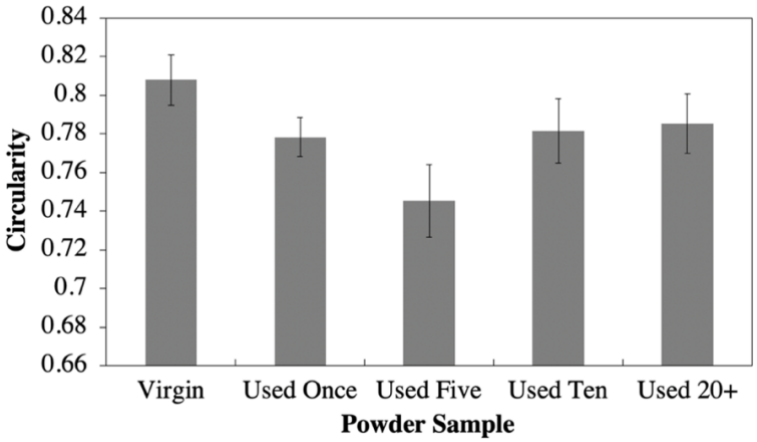

Figure 35. Circularity values of porosities from Al10SiMg SLM samples produced with various reused powder feedstock

4.3.4 Effects of Powder Reuse on SLM Microstructure

Representative microstructure from the XZ cross sections of cubic samples were compiled and are presented in Figure 36. Build direction is indicated by the black arrow. For SLM, UCF-optimized and high ED parameters, increases in porosity are observed after reuse, with the high ED parameters resulting in the most pronounced increase in porosities. Qualitatively, microstructures of SLM samples printed using low ED contain significant amounts of flaws which appear in similar quantity for all powder feedstock.

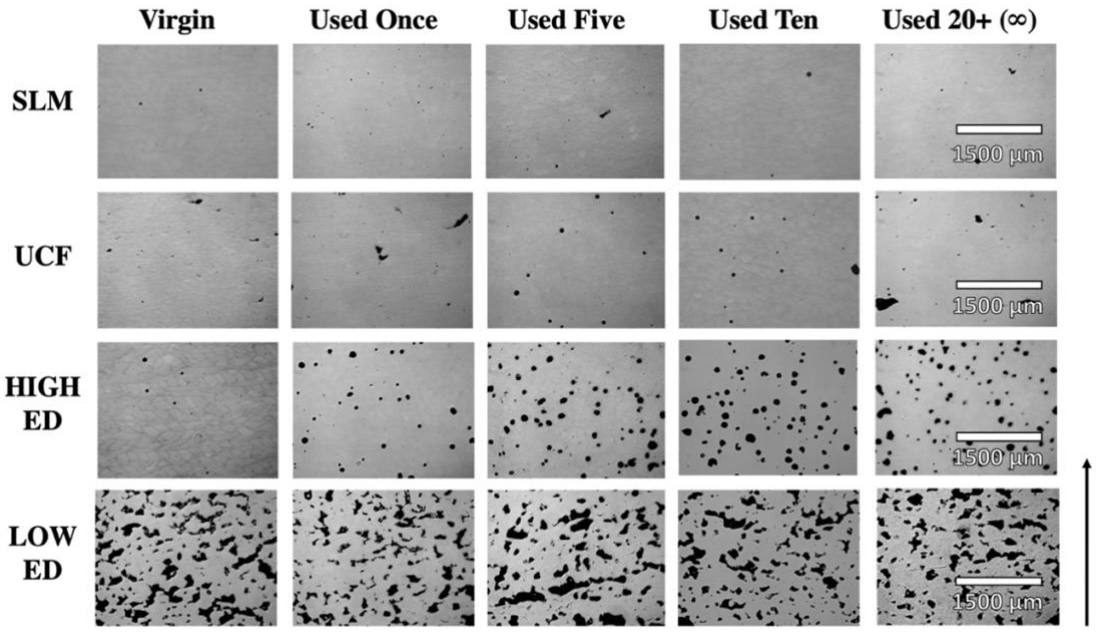

Figure 36. Optical micrographs from the XZ cross sections of Al10SiMg SLM samples fabricated with various reused powders

Porosity values for XY and XZ cross sections for all cubic samples are listed in Table 21 and graphed in Figure 37a and Figure 37b. While samples printed with SLM and UCF parameters exhibit minimal and largely insignificant variation in porosity percentage, samples printed with high and low ED exhibit seemingly positive and negative parabolic trends, respectively.

Table 21. Porosity area percentages for RPS cubic samples

Parameter Set	Powder	Porosity Area% (XY)	Porosity Area% (XZ)
SLM	Virgin	0.478 ± 0.52	0.298 ± 0.17
	Used Once	0.157 ± 0.04	0.183 ± 0.05
	Used Five	0.273 ± 0.07	0.342 ± 0.17
	Used Ten	0.109 ± 0.07	0.107 ± 0.03
	Used 20+	0.424 ± 0.07	0.107 ± 0.03
UCF	Virgin	0.437 ± 0.31	0.461 ± 0.28
	Used Once	0.834 ± 0.63	1.070 ± 0.95
	Used Five	0.576 ± 0.27	0.412 ± 0.09
	Used Ten	0.186 ± 0.07	0.289 ± 0.13
	Used 20+	0.666 ± 0.27	0.927 ± 0.54
High ED	Virgin	0.765 ± 0.44	0.519 ± 0.35
	Used Once	3.786 ± 1.26	3.684 ± 1.67
	Used Five	4.961 ± 0.84	5.348 ± 0.84
	Used Ten	6.009 ± 1.13	5.455 ± 1.02
	Used 20+	4.782 ± 1.40	4.283 ± 0.96
Low ED	Virgin	20.930 ± 2.39	23.699 ± 2.03
	Used Once	18.502 ± 2.39	18.442 ± 1.44
	Used Five	19.010 ± 3.07	16.597 ± 3.16
	Used Ten	17.798 ± 3.89	16.398 ± 3.65
	Used 20+	20.302 ± 3.11	18.723 ± 2.61

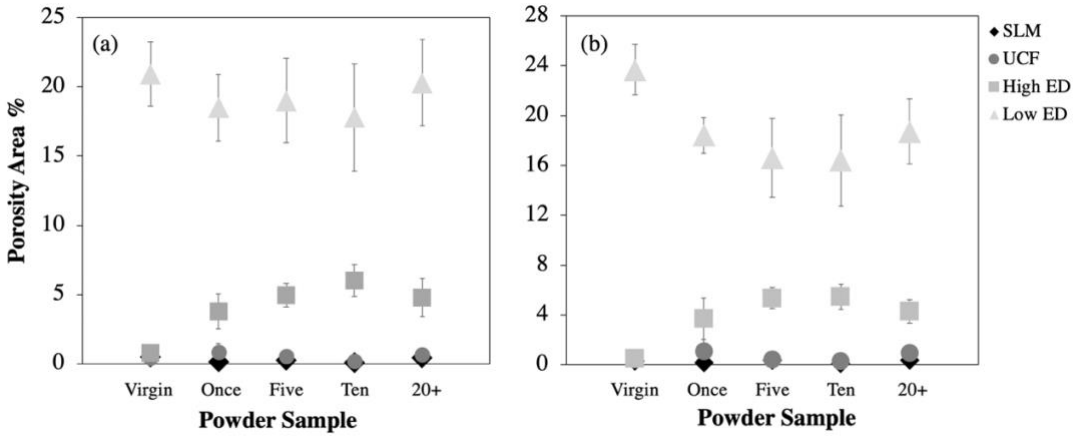

Figure 37. Porosity area percentages of Al10SiMg SLM samples as a function of reuse for (a) XY cross section and (b) XZ cross section

Measurements of melt pool depth and width were obtained for each combination of parameter set and powder sample utilized. Results are listed in Table 22 and graphed in Figure 38. Melt pool measurements for samples printed with low ED parameters are not shown. Due to the significant amount of porosity in these samples, melt pools were not visible in microstructure. When printing with SLM parameters, continual powder reuse resulted in little variation for melt pool depth and width. For UCF parameters, melt pool width does not vary significantly, while depth values vary slightly, with an outlier for "used once" powder feedstock. Increase in melt pool depth is observed when a combination of high energy density parameters and powder reuse is applied. However, melt pool width values do not appear to vary significantly in this case.

Table 22. Melt pool width and depth measurements after continued powder reuse for samples

Parameter Set	**Powder Sample**	**Melt Pool Width (µm)**	**Melt Pool Depth (µm)**
SLM	Virgin	228.39 ± 30.52	129.94 ± 24.09
	Used Once	212.96 ± 17.64	145.63 ± 24.78
	Used Five	236.32 ± 24.95	145.63 ± 24.78
	Used Ten	219.34 ± 17.01	151.80 ± 17.50
	Used 20+	209.47 ± 19.70	145.37 ± 19.54
UCF	Virgin	209.47 ± 19.70	145.37 ± 19.54
	Used Once	217.18 ± 24.80	72.94 ± 14.85
	Used Five	251.03 ± 39.79	156.89 ± 25.17
	Used Ten	240.84 ± 40.16	152.21 ± 26.37
	Used 20+	229.53 ± 23.39	84.31 ± 18.17
High ED	Virgin	275.00 ± 24.55	121.14 ± 43.96
	Used Once	292.59 ± 43.69	214.04 ± 65.71
	Used Five	308.85 ± 56.09	268.36 ± 34.23
	Used Ten	322.43 ± 24.55	260.96 ± 29.01
	Used 20+	293.42 ± 25.69	252.57 ± 30.79

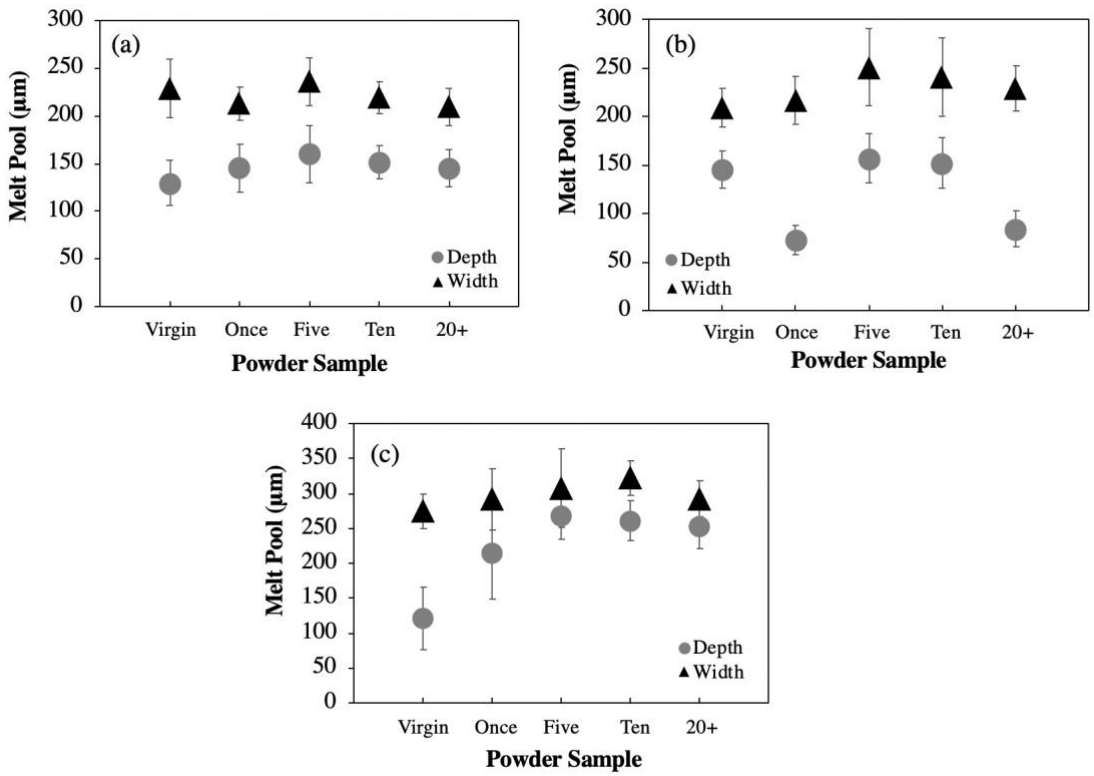

Figure 38. Melt pool geometry measurements after continued powder reuse for samples built with a) SLM, b) UCF, c) High ED parameter sets

4.3.5. Effects of Powder Reuse on Mechanical Properties of SLM Parts

Results from uniaxial tensile tests are listed with standard deviations in Table 23. Engineering stress strain curves are plotted in Figure 39. All tensile specimens for this study were printed using SLM parameter set which is detailed in Table 7. These samples, regardless of how many reuses were applied, had porosities less than 1.07% on average, as reported in Table 21. Variations in mechanical strength values are minimal for these samples, however, samples printed using virgin powders achieved the highest YS and UTS values of 252.5 ± 7.1 MPa and 453.6 ± 3.1 MPa, respectively. Consequently, highest elongation, or strain at fracture values are obtained from tensile samples printed with five times reused feedstock.

Table 23. Room temperature tensile properties with standard deviations for the Al10SiMg SLM components fabricated with various reused powder feedstock

Powder Sample	Yield Strength (MPa)	UTS (MPa)	Strain at Fracture	Modulus of Toughness
Virgin	252.5 ± 7.1	453.6 ± 3.1	0.095 ± 0.012	37.14 ± 5.28
Used Once	237.6 ± 6.2	447.7 ± 4.8	0.112 ± 0.010	44.11 ± 5.01
Used Five	241.8 ± 7.2	441.4 ± 2.1	0.119 ± 0.017	46.53 ± 7.40
Used Ten	240.9 ± 3.2	450.1 ± 3.2	0.105 ± 0.001	40.98 ± 0.78
Used 20+	252.5 ± 8.6	447.2 ± 2.6	0.114 ± 0.024	45.18 ± 10.83

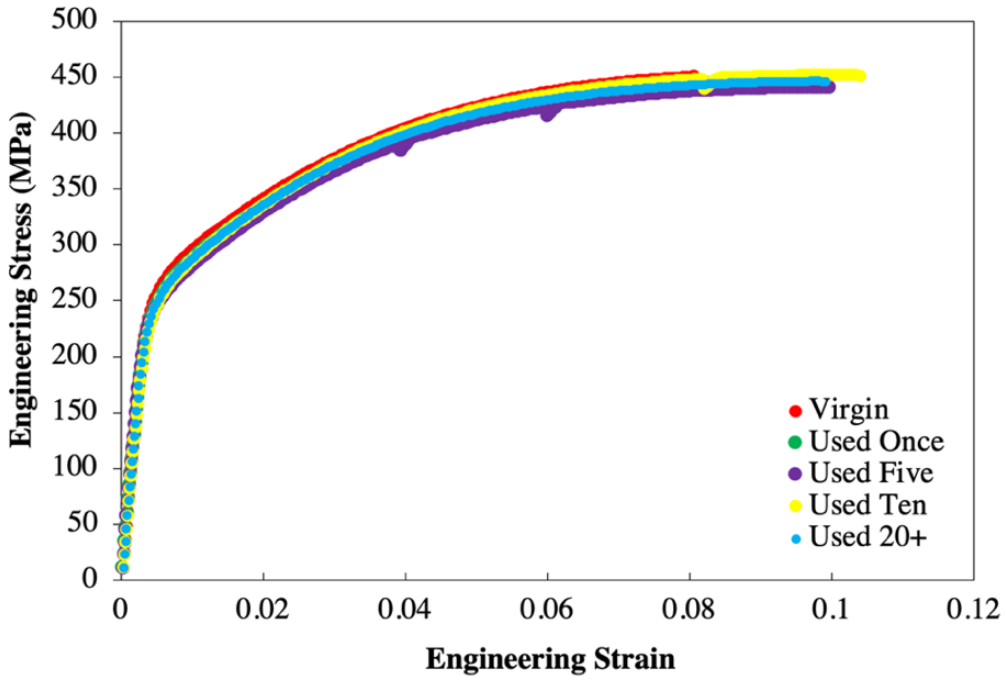

Figure 39. Engineering stress-strain curves of the Al10SiMg alloy in the as-built state for each RPS powder sample

CHAPTER 5: DISCUSSION

5.1 Gas Atomization of Al10SiMg

Results from gas atomization experiments indicated that melt flow rate was the most influential parameter with respect to Y75 and Y45 powder yields, as is demonstrated in Figure 17. By definition, primary breakup in atomization occurs in the area just below the orifice, where the high pressure gas first interacts with the molten flow entering the chamber. Larger melt droplets that are not atomized in this regime are typically broken up in the secondary breakup regime. Therefore, longer durations of melt and atomizing gas interaction in the primary breakup regime may facilitate more efficient melt break up and allow for the production of finer powders. This relationship was also observed in similar studies and were explained by similar reasonings [22]. Moreover, metal flow rate affects parameters such as metal film thickness, heat transfer between gas and molten metal and the velocity decay in the gas stream. Gretzinger *et* al. [60] have shown that the melt film thickness increases in gas-molten metal interaction zone with respect to the molten alloy flow rate. This increased film thickness will undoubtedly lead to a larger average particle size in primary breakup. In fact, in extreme cases, film thickness can inhibit droplet formation and result in the formation of unstable ligaments [60]. These often present as slag in as-atomized powder.

While melt flow rate was identified as the most influential parameter when analyzed independently, it is important to note that combined effects from gas pressure and melt properties will also affect flow characteristics. When atomizing at higher flow rates, efficient melt breakup can also be facilitated by employing higher gas pressures. This is demonstrated clearly in results obtained from gas pressure experiments. Higher gas atomization pressures led to higher powder

yields when keeping other parameters constant, as shown in Figure 18. In fact, atomization conducted with moderately high melt flow rate of 0.02 kg/s was able to produce Y75 yield of 80 wt.% with an atomizing gas pressure of 2.7 MPa, which was the highest observed Y75 yield in this study. The relationship between high gas pressures and powder refinement in atomization is assumed to be a result of the increased gas flow kinetic energy associated with increasing gas pressures [61]. Gas pressures will affect properties like gas flow rate, velocity, and length of supersonic zone in the gas stream. Several models for droplet formation in planar sprays have been used to describe the mechanism of melt breakup and subsequent powder production in gas atomization. A two-fluid jet instability model described by Dombrowski *et* al. [62] postulates that interaction in the gas-melt coupling zone (equivalent to the primary breakup regime for gas atomization) amplify "surface waves" within the liquid which grow until a critical size is achieved and breakup is initiated. See *et* al. [63] confirmed this experimentally through a series of low-pressure gas atomization experiments and found that melt breakup was initiated near the focal point of the gas stream. While these studies do not specifically address particle size refinement, they illustrate the significant role of gas flow in droplet formation. However, Anderson *et* al. [64] went on to investigate the process dynamics for gas atomization in high pressure atomization and explored nozzle geometries which minimized gas flow energy losses. Their results showed that supersonic gas flow associated with high gas pressures led to subsequent powder refinement.

Melt temperature experiments were conducted with constant pressure of 2.04 ± 0.009 MPa and melt flow rate of 0.034 ± 0.003 kg/s for range of temperatures 850 to 1000°C. For this parameter set, the highest Y75 yield achieved was 43 wt.%, which is listed in Table 11. For the gas atomization of metal alloys, melt temperature can affect particle size through (1) variation of

molten liquid properties with increase in temperature and (2) premature solidification of the material [22]. From thermodynamics, it is intuitive that increased temperatures result in decreased surface tension and viscosity of a material. Therefore, higher melt temperatures are expected to facilitate metal break-up during atomization due to decreased viscosity of the melt and allow for the production of finer powders. However, when atomization temperature is insufficient for melting, solidification of the material may occur before breakup takes place. In extreme cases, this premature solidification can cause nozzle blockage and ultimately result in "failed-run" of atomization. For atomization experiments conducted with varying melt temperature, minimal increases were in fact observed with increasing melt temperature, as is depicted in Figure 19. In free-fall configuration atomization systems, similar to the system employed in this thesis, superheat temperature is also shown to affect powder morphology [25].

Ultimately, findings from literature and results presented in this thesis clearly indicate that the combined effects of melt flow rate, gas pressure and melt temperature should be considered when conducting particle-size tailored atomization. Independently, increasing melt flow rate was found to cause significant decreases in powder yield due to decreased melt and gas flow interaction. Gas pressure and melt temperature parameters were shown to impact particle size due to their effects on the breakup behavior and viscosity of the molten stream, respectively.

Following gas atomization, Al10SiMg powders were cross-sectioned and used to carry out several microstructural characterizations. These characterizations included quantification of porosities and particle diameters. Measured particle diameters were used in a convection heat transfer model to estimate the cooling rates of powders in gas atomization. While porosities were not overall significant for Al10SiMg powders, Figure 21 shows that the percentage of porosities

was largest for large particle size fractions. Porosities were found to consistently decrease with decreasing particle size which is in agreement with results from previous studies [65, 66]. Formation of porosities in gas atomized powders are typically said to form as a result of entrapped gas during the solidification process. The relationship between porosity and particle size is highly influenced by liquid breakup behavior [65], where larger ligaments tend to entrap larger amounts of gas, a phenomena which can be described by the bag break-up mechanism first described by Rabin *et* al. [67] in 1990. The bag break-up mechanism is illustrated in Figure 40 below.

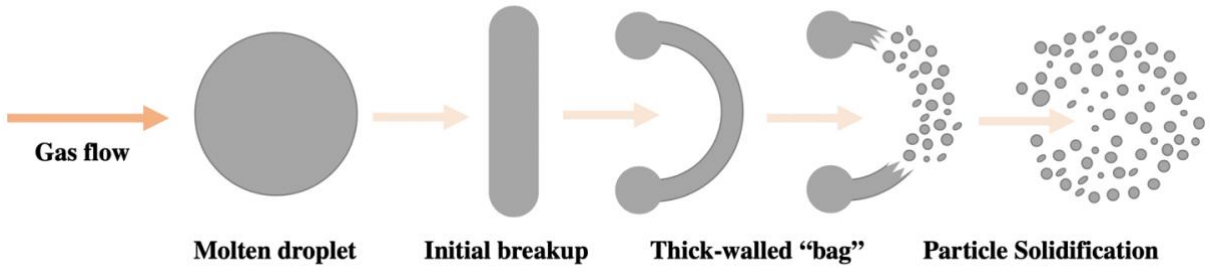

Figure 40. Schematic of the bag break-up mechanism proposed by Rabin *et* al. *[67]*

Particle diameter measurements of Al10SiMg powder were used in conjunction with a convection heat transfer model proposed by Shiwen *et* al. [53] to estimate powder cooling rates. Application of this model resulted in cooling rates of 6.3×10^{6} K/s to 5.5×10^{3} K/s for powders with diameter of 4.3 µm to 146.3 µm, respectively. Figure 26 presents the cooling rate curve as a function of particle diameter for powders produced in this study. While these cooling rates are within the range reported by other studies [57, 58], limitations and error margins of this model must be considered. As stated by Shiwen *et* al. [53] this model is simplified and makes several assumptions which include the production of perfectly spherical particles in the process and constant velocity field of gas flow. These assumptions may lend the model to certain degrees of

error. Despite this fact, Shiwen *et* al. [53] reported excellent agreement between simulated and experimental results. Shulka *et* al. [68] presented another method for estimating the cooling rates of atomized powder. Their method utilizes a heat flux balance combined with classical heterogeneous nucleation theory to estimate both cooling rate and undercooling of droplets in an atomization spray as a function of droplet diameter. Shulka *et* al. [68] reported estimated cooling rates of 7×10^4 K/s for powders with diameter of 40 μm but found discrepancies between simulated and experimental results. From discussion of these methodologies for estimating powder cooling rates it is clear that factors such as coalescence, gas and melt temperature, and differential velocity should be considered for most accurate estimations.

5.2 SLM Studies with the Al10SiMg Alloy

To determine the optimal particle size distribution for Al10SiMg feedstock in SLM, samples were printed using five different particle size distributions which had average particle size of 33.03 μm, 42.28 μm, 44.19 μm, 68.98 μm and 92.80 μm. The effects of particle size were analyzed for SLM samples with respect to microstructure, density, hardness and tensile properties. From observation of powder morphology, feedstock with larger average particle size appeared to exhibit slightly more irregularity and satellites. This observation was also made in similar studies [69, 70] and is inherent to the manufacturing method, e.g. gas atomization, water atomization, etc. Consideration for particle distribution in LPBF processes arise from its subsequent effects on powder bed formation, layer density and fusion/sintering kinetics [31]. While all particle size distributions in this study were able to print successfully, it is clear that certain particle size distributions, i.e., those with too small or too large of a distribution, can cause variation in powder

bed and layer densities which can lead to adverse effects in printed components when the LPBF parameters deviate from optimum. This is important to consider especially for components with varying geometries where optimum LPBF parameters employed may be transferred into energy input differently in regard to melting and solidification (i.e., energy and heat transfers).

Results from Archimedes' principle and image analysis revealed similar relative density and porosity area percentages in SLM samples for all particle size distributions. As evidenced by data listed in Table 15 and Table 16, all samples resulted in over 99% density; and similar amounts of porosity were observed in samples printed with variable particle size distribution. Both Archimedes' principle and image analysis are commonly used characterization methods employed for the analysis of SLM samples and have been shown to produce repeatable results with little margin of error [71]. Effects of particle size distribution on SLM part density is often considered in conjunction with resultant factors like layer and powder bed density. Liu *et* al. [72] utilized various particle size distributions coupled with a variety of laser scan strategies and found that reduced powder bed density associated with smaller powder size distributions led to slight decreases in subsequent part density. As is demonstrated in Figure 29, samples printed using feedstock with smaller distributions, e.g. 33.03 µm and 42.28 µm, had smallest density values.

Despite similar relative density and porosity values, interestingly, samples printed with 92.80 µm powders resulted in the largest Vickers hardness (125), yield strength (265 MPa) and ultimate tensile strength (448 MPa) in this study. Feedstock with average particle size of 92.80 µm had the narrowest size distribution suggesting a link between tighter size distributions and high strength components. This may be due to factors such as packing fraction and powder flowability. In fact, a large presence of small particles in feedstock has been shown to negatively affect powder

bed density and flowability due to higher interparticle friction [73], properties which have been proven to negatively affect component density. Evidence of this behavior is supported by data in Table 18 where 33.03 µm feedstock resulted in the lowest yield and ultimate tensile strength values. There is evidence that multi-modal powder samples, i.e., samples containing both small and large particles also have beneficial effects on part density. German [31] proposed that the optimum mixture for AM corresponds to two-thirds large powder and one-third small powder. Therefore, the use of narrow size distribution and mixture of moderate size (75 µm) and larger particles (106 µm), may explain the observation of higher mechanical strength values for the 92.80 µm sample. Results from this study and evidence from literature demonstrate that particle size distribution is an important factor in the resulting density and mechanical properties of SLM components. However, it should be noted that the most optimal components are printed with a combination of appropriate particle size, layer thickness, beam diameter and flowability [72].

In addition, samples were printed with variably recycled feedstock to identify the critical reuse limit of Al10SiMg powders. A parameter matrix outlined in Table 7 was used to print samples using powders which had been reused zero, one, five, ten and over twenty times. Image analysis was used to measure the particle size and circularity of powders after each reuse. Original powder feedstock had particle size distribution of 20 µm to 63 µm. Image analysis of powder samples revealed average particle size increased from 42.5 µm to 84.2 µm after over twenty uses. This dramatic increase was identified to be the result of an increased number of coalesced particles in recycled powders, which provides evidence for the need of sieving between consecutive reuses. While circularity values did not vary significantly for powders, measurements revealed virgin powders to be the most circular. Maamoun *et* al. [74] observed similar results in their recycled

powder but found that such small differences in powder morphology did not significantly affect fabricated part quality.

Microstructural characterization of samples produced with recycled powders included quantification of porosity, and measurements of melt pool width and depth. For optimized laser parameters (i.e., SLM and UCF parameter sets) powder reuse contributed to little variation in porosity. However, for high ED and low ED parameter sets, powder reuse caused significant variations in porosity. To elaborate, when printing using high ED parameters, powder reuse caused porosity area percentage to increase from 0.765% to 6.01% and using low ED parameters caused porosity area percentage to decrease from 20.93% to 17.798%. These trends can be observed in Figure 37. Extensive measurement of melt pool geometries found that when coupled with high ED parameters, recycling powders caused melt depth to increase from 275 µm to 322 µm. This variation in porosity and increased melt depth is believed to be due to increased levels of oxides in Al10SiMg after recycling. Previous studies [75, 76] have observed increased levels of oxides in powders after recycling caused by exposure to laser and prolonged exposures to oxygen when recycled. The increased presence of oxides in feedstock effect laser absorption in that oxidized surfaces tend to absorb laser radiation within the surface oxide layers [77]. This is caused by the interference phenomena which occurs inside the oxide layer. The laser beam is partly absorbed and will reflect at the surface, with the remaining light reflecting between the metal and oxide-atmosphere boundary [77]. This phenomenon is depicted graphically in Figure 41. While some amount of oxides are inherent to metallic alloys, careful control of powders should be taken to limit further oxidation, i.e., humidity control and reducing exposure to oxygen when storing

powder, as oxide layers can cause increases in laser absorptivity by as much as an order of magnitude [78].

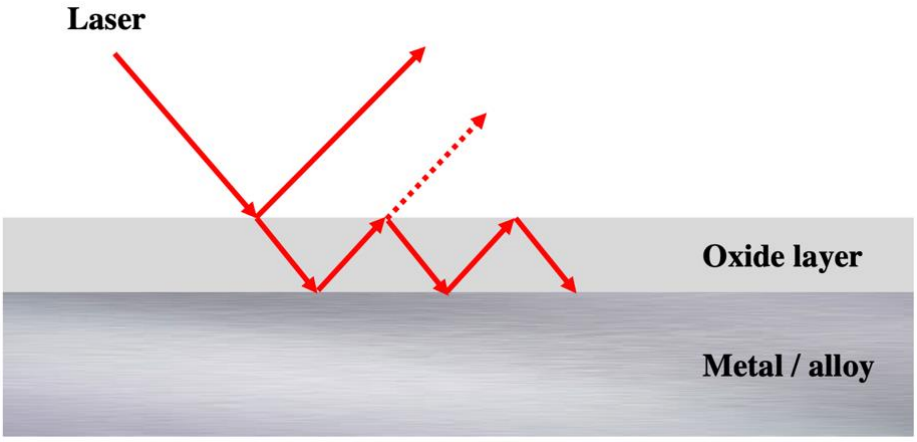

Figure 41. Schematic of laser absorption in oxide layer of metal alloy

By definition of energy density shown in Eq. (1), the increased laser absorptivity associated with oxides will increase the transfer efficiency of the overall energy density into the powder bed. This relationship explains the observations of increased porosity when printing with recycled powder and high ED parameters (i.e., more keyhole pore formation) and reduced porosity when printing with recycled powder and low ED parameters (reduction of lack-of-fusion pores). The reason this is not observed for samples printed with SLM and UCF samples is most likely due to the application of optimized laser parameters and large processing window for Al10SiMg [15]. Contrarily, high ED and low ED parameters were able to exacerbate this absorption effect which presented in the microstructure as significant variations in porosities. Therefore, evidence from literature and results from this study prove that increased laser absorptivity values associated with increased oxide scale in recycled powders will cause variation in porosity formation with respect to the applied laser parameters for the LPBF of Al10SiMg.

Powder feedstock was then used to print tensile specimen using the “SLM” parameter set detailed in Table 7, which is a parameter matrix that has been optimized for the Al10SiMg alloy. Although tensile strength values did not vary significantly when recycled powders were used, the highest yield strength and ultimate tensile strength values of 252 MPa and 453 MPa were observed when using virgin powder feedstock. Highest elongation value of 12% resulted from samples printed with five times reused powder. These results suggest that when using optimized laser parameters, Al10SiMg alloy powders can be reused up to twenty times without suffering significant variation to mechanical strength. In fact, tensile samples printed using twenty times reused powder had similar mechanical properties to those printed with virgin powder. As evidenced in Table 21 and Table 22 specimen fabricated using recycled powders and “SLM” optimized laser parameter set showed little variation in porosity and melt pool geometry when printing with optimized parameters. Therefore, with no significant amounts of porosities in any tensile specimen, large variations in mechanical properties were not expected.

CHAPTER 6: SUMMARY AND CONCLUSIONS

6.1 Optimal Gas Atomization Parameters for Al10SiMg

Series of gas atomization experiments were conducted with variable melt flow rate, gas pressure and melt temperature to identify the relationship between processing parameters and powder yield and characteristics. Melt flow rate experiments were conducted with flow rates in the range of 0.014 to 0.036 kg/s, melt temperature of 950°C and gas pressure of 2.0 MPa. At constant gas pressure and melt temperature, Y75 and Y45 powder yields were found to increase with decreasing melt flow rates. Gas pressure experiments were conducted with pressures in the range of 1.4 – 3.1 MPa, melt flow rate of 0.0195 kg/s, and melt temperature of 950°C. Melt temperature experiments were conducted with melt temperatures in the range of 850 – 1000°C, melt flow rate of 0.034 kg/s and 2.04 MPa. For both gas pressure and melt temperature variable atomization runs, minimal increases in powder yield were observed for higher gas pressures and melt temperatures. The highest Y75 powder yield for this study was achieved using a combined parameter matrix of 2.7 MPa gas pressure, 0.020 kg/s melt flow rate and melt temperature of 950°C. While melt flow rate was shown to be the most influential on powder yield, results from this study suggest that particle size-tailored atomization requires an optimized combination of processing parameters. Porosity area percentages and particle diameters were measured from cross-sectioned powders. While presence of porosities in Al10SiMg powders were overall insignificant, porosities were observed in higher quantity for larger particles. Measured particle diameters were used to calculate SDAS. These measurements were also coupled with a convection heat transfer model to estimate cooling rates for Al10SiMg powders. Particles with diameter from

4.3 µm to 146.3 µm had SDAS and estimated cooling rates in the range of 0.74 µm to 6.3 µm and 6.3×10^{6} kg/s to 5.5×10^{3} kg/s, respectively.

6.2 Optimal Particle Size Distribution for SLM of Al10SiMg

To determine the optimal particle size distribution for Al10SiMg powder feedstock in the SLM process, cubic and tensile samples were printed using optimized laser parameters and each of the following five particle size distributions: ≤ 45µm, 20µm ≤ x < 63µm, ≤ 75µm, ≤ 106µm and 75µm ≤ x < 106µm. These five distributions had average particle size of 33.03 µm, 42.28 µm, 44.19 µm, 68.98 µm and 92.80 µm, respectively. Morphology of powder feedstock was observed for each size distribution. In general, irregular particles were more frequently observed in larger size distribution powder samples. Archimedes' principle experiments were employed to experimentally determine the relative density of cubic samples. All samples were found to have relative density of over 99%. However, results from image analysis of cubic SLM sample cross sections indicated that samples printed with average particle size of 42.28 µm had least amount of porosity. Mechanical testing of samples indicated minimal variation in Vickers hardness with respect to variable particle size feedstock. However, hardness values were highest in cubic samples printed with average particle size of 92.80 µm. Interestingly, this powder sample also resulted in the highest yield strength and UTS values of 265 MPa and 448 MPa, respectively. These results were attributed to the narrow particle size distribution and multimodal nature of powder feedstock, i.e., mixture of moderate and large particles found in the 92.80 µm feedstock.

6.3 Powder Recycling of Al10SiMg in the SLM Process

In order to identify the critical reuse limit of Al10SiMg powder feedstock in the SLM process, various laser parameter sets were used to print cubic and tensile samples with powder feedstock that had been reused zero, one, five, ten and over twenty times. After each use in the SLM process, samples containing recycled and condensate powders were collected from the build platform and overflow bottles. Particle size was found to increase significantly after continued use due to exposure to laser radiation. These results emphasize the importance of sieving powders after reuse to maintain original size distribution and eliminate agglomerated powders. Increased powder reuse was found to have minimal effects on part microstructure when printing with optimized laser parameters. However, when using high ED parameters, increasing powder reuse led to significant increases in porosity. Additionally, measurements of as-printed melt pool geometry revealed that melt pool depths increased from 275 to 322 μm after ten uses when printing with high ED parameters. These results are believed to be due to the increased laser absorptivity associated with increased oxides typically found in recycled powders. Tensile specimens were printed using optimized SLM parameters for each powder feedstock. These tests revealed minimal variation of yield strength and ultimate tensile strength values after continued reuse, which indicate Al10SiMg powders can be reused without sacrificing quasi-static tensile properties, when coupled with optimized laser parameters. This was due to the insignificant variation in porosity and melt pool geometry for samples printed with optimized parameters.

CHAPTER 7: RECOMMENDATIONS FOR FUTURE WORK

Optimization studies for the gas atomization and selective laser melting of Al10SiMg were explored in this thesis. Due to the highly variable nature of both the gas atomization and selective laser melting processes, further studies should be conducted in order to expand on the observations made in this thesis. Additionally, in order to develop a more comprehensive and universally applicable gas atomization and selective laser melting strategy, i.e. applicable to more alloy systems and SLM machines, the following recommendations for future work are presented.

With respect to the gas atomization process, the parametric study conducted is specific to free fall close-coupled gas atomization systems and the Al10SiMg alloy. While the experiments conducted in this thesis are sufficient to provide a basis for particle size tailored atomization – optimization for post-process properties like surface morphology and satellites was not identified. Studies like those conducted by Singh *et* al. [25] demonstrated that parameters such as apex angle of atomizer, superheat of liquid metal and diameter of metal delivery tube (orifice) can affect the morphology of atomized powders. Investigations for surface morphology tailored gas atomization processes may prove beneficial as both particle size and morphology have been identified by researchers as influential factors in SLM [34]. Expansion of this research to include multiple alloy systems will require, above all, analysis of superheat temperatures required to achieve the optimal surface tension and viscosity values necessary for successful atomization [22].

While the effects of particle size distribution on SLM components was examined in this thesis, considerations of powder flowability were not thoroughly investigated. Expanding on this research, the relationship between particle size distribution and feedstock flowability may be an interesting addition to this work. Any of the following powder flowability characterization can be

conducted; Hall flowmeter testing, measurement of Hausner ratio and revolution powder analysis [79]. In addition to particle size distribution, several studies have shown that particle shapes contribute significant effects on absorptivity, layer density and subsequent part density [34]. This is true not only for Al10SiMg but other commonly used alloys in SLM such as Ti6Al4V [49]. Furthermore, the combined effects of slice thickness, powder bed density and laser beam diameter were not explored in this thesis. As such, future investigations of this factor in addition to particle geometry and balling effects for the SLM process may be warranted.

Results from this thesis also found that recycled powders may not be detrimental to mechanical properties when printing with optimized parameters. However, as was demonstrated in the results section, recycling powders can introduce significant porosities when printing with high ED or low ED parameters, that do not appear when utilizing virgin powder. Currently this is believed to be a result of larger oxide scale in reused powder, which contribute to larger absorptivity values. This increase in absorptivity, combined with high ED parameters is believed to be the cause of additional porosities observed after continued reuse, however, this hypothesis remains untested in this work. More importantly, increase in porosities associated with increased reuse and non-optimal parameters will undoubtedly contribute to detrimental effects in mechanical applications. Additionally, more efficient energy transfer into the powder bed, associated with increases in laser absorptivity, may facilitate the evaporation of light elements, i.e., Al, Mg. Therefore, in future work, measurement of oxide scale thickness in reused powders, analyses of the relationship between oxidation and laser absorptivity for Al10SiMg, compositional analysis of SLM specimen, and thorough investigations of the mechanisms behind the increase in porosities may reveal insightful results.

REFERENCES

[1] K. Arachchilage, M. Haghshenas, S. Park, L. Zhou, Y. Sohn, B. McWilliams, K. Cho and R. Kumar, "Numerical simulation of high-pressure gas atomization of two-phase flow: Effect of gas pressure on droplet size distribution," *Advanced Powder Technology,* vol. 30, pp. 2726 - 2732, 2019.

[2] S. Motaman, A. Mullis, R. Cochrane and D. Borman, "Numerical and Experimental Investigations of the Effect of Melt Delivery Nozzle Design on the Open-to Closed-Wake Transition in Closed-Coupled Gas Atomization," *Metallurgical and Materials Transactions B*, vol. 46, pp. 1990 - 2004, 2015.

[3] I. Polmear, Light Alloys: Metallurgy of the Light Metals, London: Arnold, 1995.

[4] J. R. Davis, Alloying: Understanding the Basics, ASM International, 2001.

[5] K. H. Kumar, N. Chakraborti, H. Lukas, O. Bodak and L. Rokhlin, "Al-Mg-Si (Aluminum - Magnesium - Silicon)," in *Light Metal Systems. Part 3*, Stuttgart, SpringerMaterials, 2005.

[6] L. Heusler and W. Schneider, "Influence of alloying elements on the thermal analysis results of Al-Si cast alloys," *Journal of Light Metals 2,* pp. 17 - 26, 2002.

[7] J. Murray and A. McAlister, "The Al-Si (Aluminum-Silicon) system," *Bulletin of Alloy Phase Diagrams*, vol. 5, no. 74, 1984.

[8] A. Dahle, P. Tondel, C. Paradies and L. Arnberg, "Effect of grain refinement on the fluidity of two commercial Al-Si foundry alloys," *Metallurgical and Materials Transactions A*, vol. 27, pp. 2305 - 2313, 1996.

[9] A. Sharma and J. P. Jung, "Possibility of Al-Si Brazing Alloys for Industrial Microjoining Applications," *Journal of the Microelectronics and Packaging Society,* vol. 24, no. 3, pp. 35 - 40, 2016.

[10] M. Zamani, Al-Si Cast Alloys - Microstructure and Mechanical Properties at Ambient and Elevated Temperature, Jonkoping: School of Engineering, Jonkoping University, 2015.

[11] M. Schoenitz and E. Dreizin, "Structure and Properties of Al-Mg mechanical alloys," *Journal of Materials Research,* vol. 18, no. 8, pp. 1827 - 1836, 2003.

[12] G. Anne, M. Ramesh, H. S. Nayaka, S. B. Arya and S. Sahu, "Development and characteristics of accumulative roll bonded Mg-Zn/Ce/Al hybrid composite," *Journal of Alloys and Compounds,* vol. 724, pp. 146 - 154, 2017.

[13] S. Zahi and A. Daud, "Phase Diagram, Thermodynamics and Microstructure of Al-Mg System," in *International Electronic Manufacturing Conference*, 2010.

[14] A. Mishra, "Friction Stire Welding of Dissimilar Metal: A Review," *International Journal for Research in Applied Science & Engineering Technology (IJRASET),* vol. 6, no. 1, pp. 2321 - 9653, 2018.

[15] L. Zhou, A. Mehta, E. Schulz, B. McWilliams, K. Cho and Y. Sohn, "Microstructure, precipitates and hardness of selectively laser melted AlSi10Mg alloy before and after heat treatment," *Materials Characterization,* vol. 143, pp. 5 - 17, 2018.

[16] D. Herzog, V. Seyda, E. Wycisk and C. Emmelmann, "Additive manufacturing of metals," *Acta Materialia,* vol. 117, pp. 371 - 392, 2016.

[17] L. Thijs, K. Kempen, J. Kruth and J. Humbeeck, "Fine-structured aluminum products with controllable texture by selective laser melting of pre-alloyed AlSi10Mg powder," *Acta Materialia,* vol. 61, no. 5, pp. 1809 - 1819, 2013.

[18] Renishaw, *AlSi10Mg-0403 powder for additive manufacturing,* Staffordshire, UK, 2015.

[19] N. Aboulkhair, C. Tuck, I. Ashcroft, I. Maskery and N. Everitt, "On the Precipitation Hardening of Selective Laser Melted AlSi10Mg," *Metallurgical and Materials Transactions A,* vol. 46, no. A, 2015.

[20] H. Lu, Science and Engineering of Droplets, William Andrew Inc., 1999.

[21] K. J. Buschow, R. Cahn, M. Flemings, B. Ilschner, E. Kramer, S. Mahajan and P. Veyssiere, Encyclopedia of Materials: Science and Technology, Elsevier Ltd., 2001.

[22] A. Unal, "Effect of processing variables on particle size in gas atomization of rapidly solidified aluminum powders," *Materials Science and Technology,* vol. 3, pp. 1029 - 1039, 1987.

[23] G. Janowski, F.S.B. and S. Ridder, "Beneficial Effects of Nitrogen Atomization on an Austenitic Stainless Steel," *Metallurgical Transactions,* vol. 23, no. A, pp. 3263 - 3272, 1992.

[24] R. VanStone, F. Rizzo and J. Radavich, in *Proc. 2nd Int. Conf. on Rapid Solidification Processing, Principles and Applications*, Reston, VA, Claitor's Publishing Division, 1980, pp. 260 - 272.

[25] D. Singh and S. Dangwal, "Effects of process parameters on surface morphology of metal powders produced by free fall gas atomization," *Journal of Materials Science,* vol. 41, pp. 3853 - 3860, 2006.

[26] O. Nichiporenko and Y. Naida, "Heat exchange between metal particles and gas in the atomization process," *Theory, Production Technology, and Properties of Powders,* vol. 7, pp. 509 - 512, 1968.

[27] J. See and G. Johnston, "Interactions between nitrogen jets and liquid lead and tin streams," *Powder Technology,* vol. 21, no. 1, pp. 119 - 133, 1978.

[28] K. W. A. G. W. Meiners, "Shaped body especially prototype or replacement part production". Germany Patent DE19649865C1 , 02 December 1996.

[29] American Society for Testing and Materials (ASTM), "Standard Guide for Additive Manufacturing - General Principles - Terminology; ASTM F2792-10e1," ASTM-ISO, West Conshohocken, PA, 2012.

[30] L. Dobrazanski, A. Dobrzanska-Danikiewicz, T. Gawel and A. Achtelik-Franczak, "Selective Laser Sintering and Melting of Pristine Titanium and Titanium Ti6Al4V Alloy Powders and Selection of Chemical Environment for Etching of Such Materials," *Archives of Metallurgy and Materials,* vol. 60, no. 3A, pp. 2040 - 2045, 2015.

[31] R. German, Powder Metallurgy Science, Princeton, NJ: Metal Powder Industries Federation, 1994.

[32] G. Yablokova, M. Speirs, J. V. Humbeeck, J.-P. Kruth, J. Schrooten, R. Cloots, F. Boschini, G. Lumay and J. Luyten, "Rheological behavior of β-Ti and NiTi powders produced by

atomization for SLM production of open porous orthopedic implants," *Powder Technology,* vol. 283, pp. 199 - 209, 2015.

[33] Q. Nguyen, M. S. Nai, Z. Zhu, C.-N. Sun, J. Wei and W. Zhou, "Characteristics of Inconel Powders for Powder-Bed Additive Manufacturing," *Engineering,* vol. 3, pp. 695 - 700, 2017.

[34] K. Riener, N. Albrecht, S. Ziegelmeier, R. Ramakrishnan, L. Haferkamp, A. Spierings and G. Leichtfried, "Influence of particle size distribution and morphology on the properties of the powder feedstock as well as of Al10SiMg parts produced by laser powder bed fusion (LPBF)," *Additive Manufacturing,* vol. 34, 2020.

[35] N. Pohlman, J. Roberts and M. Gosner, "Characterization of titanium powder: Microscopic views and macroscopic flow," *Powder Technology,* vol. 228, pp. 141 - 148, 2012.

[36] D. Buchbinder, W. Meiners, K. Wissenbach and K. Muller-Lohmeier, "Rapid manufacturing of aluminum parts for serial production via Selective Laser Melting (SLM)," in *International Conference on Rapid Manufacturing,* Loughborough, 2008.

[37] A. Spierings, N. Herres and G. Levy, "Influence of the particle size distribution on surface quality and mechanical properties in AM steel parts," *Rapid Prototyping Journal,* vol. 17, no. 3, pp. 195 - 202, 2011.

[38] A. Alfaify, J. Hughes and K. Ridgway, "Critical evaluation of the pulsed selective laser melting process when fabricating ti64 parts using a range of particle size distributions," *Additive Manufacturing,* vol. 19, pp. 197 - 204, 2018.

[39] G. Jacob, C. Brown, A. Donmez, S. Watson and J. Slotwinski, "Effects of powder recycling on stainless steel powder and built material properties in metal powder bed fusion processes," *NIST Advanced Manufacturing Series 100-6,* 2017.

[40] V. P. Jr., A. Katz-Demyanetz, A. Garkun and M. Bamberger, "The effect of powder recycling on the mechanical properties and microstructure of electron beam melted Ti-6Al-4V specimens," *Additive Manufacturing,* vol. 22, pp. 834 - 843, 2018.

[41] R. O'Leary, R. Setchi, P. Prickett and G. Hankins, "An Investigation into the Recycling of Ti-6Al-4V Powder Used Within SLM to Improve Sustainability," *InImpact: Journal of Innovation Impact,* pp. 377 - 388, 2015.

[42] L. Ardila, F. Garciandia, J. Gonzalez-Diaz, P. Alvarez, A. Echeverria, R. D. M.M. Petite and J. Ochoa, "Effect of IN718 Recycled Powder Reuse on Properties of Parts Manufactured by Means of Selective Laser Melting," *Physics Procedia,* vol. 56, pp. 99 - 107, 2014.

[43] H. Asgari, C. Baxter, K. Hosseinkhani and M. Mohammadi, "On microstructure and mechanical properties of additively manufactured AlSi10Mg_200C using recycled powder," *Materials Science & Engineering A,* vol. 707, pp. 148 - 158, 2017.

[44] EOS GmbH - Electro Optical Systems, "EOS Aluminum AlSi10Mg_200C: Material data sheet," 2013, Munich.

[45] N. Read, W. Wang, K. Essa and M. Attallah, "Selective laser melting of Al10SiMg alloy: Process optimization and mechanical properties development," *Materials & Design,* vol. 65, pp. 417 - 424, 2015.

[46] K. Kempen, L. Thijs, J. Humbeeck and J.-P. Kruth, "Mechanical Properties of Al10SiMg Produced by Selective Laser Melting," *Physics Procedia,* vol. 39, pp. 439 - 446, 2012.

[47] L. Cordova, M. Campos and T. Tinga, "Revealing the Effects of Powder Reuse for Selective Laser Melting by Powder Characterization," *JOM,* vol. 71, pp. 1062 - 1072, 2019.

[48] G. Gaustad, E. Olivetti and R. Kirchain, "Improving aluminum recycling: A survey of sorting and impurity removal technologies," *Resources, Conservation and Recycling,* vol. 58, pp. 79 - 87, 2012.

[49] P. Carrion, A. Soltani-Tehrani, N. Phan and N. Shamsaei, "Powder Recycling Effects on the Tensile and Fatigue Behavior of Additively Manufactured Ti-6Al-4V Parts," *JOM,* vol. 71, no. 3, pp. 963 - 973, 2019.

[50] M. Tang, "Inclusions, Porosity, and Fatigue of Al10SiMg Parts Produced by Selective Laser Melting," Carnegie Mellon University, Pittsburgh, PA, 2017.

[51] R. German, Powder metallurgy science, Princeton, NJ, 1984.

[52] J. Sarreal and G. Abbaschian, "The effect of solidification rate on microsegregation," *Metallurgical Transactions A,* vol. 17, pp. 2063 - 2073, 1986.

[53] H. Shiwen, L. Yong and G. Sheng, "Cooling Rate Calculation of Non-Equilibrium Aluminum Alloy Powders Prepared by Gas Atomization," *Rare Metal Materials And Engineering,* vol. 38, pp. 353 - 356, 2009.

[54] EOS GmbH - Electro Optical Systems, "EOS Aluminum AlSi10Mg Material data sheet," 2009.

[55] ASTM International, "ASTM E1461-13, Standard Test Method for Thermal Diffusivity by the Flash Method," ASTM International, West Conshohocken, PA, 2013.

[56] "Nitrogen - Thermal Conductivity," The Engineering ToolBox, [Online]. Available: https://www.engineeringtoolbox.com/nitrogen-N2-thermal-conductivity-temperature-pressure-d_2084.html. [Accessed May 2020].

[57] B. Zheng, Y. Lin, Y. Zhou and E. Lavernia, "Gas Atomization of Amorphous Aluminum Powder: Part II. Experimental Investigation," *Metallurgical and Materials Transactions B,* vol. 40, pp. 995 - 1004, 2009.

[58] D. Dube, A. Couture, Y. Carbonneau, M. Fiset, R. Angers and R. Tremblay, "Secondary dendrite arm spacings in magnesium alloy AZ91D: from plaster moulding to laser remelting," *International Journal of Cast Metals Research,* vol. 11, pp. 139 - 144, 1998.

[59] S. Moylan, J. Slotwinski, A. Cooke, K. Jurrens and M. Donmez, "Lessons Learned in Establishing the NIST Metal Additive Manufacturing Laboratory," NIST, June 2013.

[60] J. Gretzinger and W. M. Jr., "Characteristics of pneumatic atomization," *AlChE,* vol. 7, no. 2, pp. 312- 318, 1961.

[61] S. Small and T. Bruce, "The comparison of characteristics of water and inert gas atomized powders," *International Journal of Powder Metallurgy,* vol. 4, no. 3, pp. 7 - 17, 1968.

[62] N. Dombrowski and W. Johns, "The aerodynamic instability and disintegration of viscous liquid sheets," *Chemical Engineering Science,* vol. 18, no. 3, pp. 203 - 214, 1963.

[63] J. See, J. Runkle and T. King, "The Disintegration of Liquid Lead Streams by Nitrogen Jets," *Metallurgical Transactions,* vol. 4, no. 11, pp. 2669 - 2673, 1973.

[64] I. Anderson, R. Figliola and H. Morton, "Flow mechanisms in high pressure gas atomization," *Materials Science and Engineering A,* vol. 148, pp. 101 - 114, 1991.

[65] G. Chen, Q. Zhou, S. Zhao, J. Yin, P. Tan, Z. Li, Y. Ge, J. Wang and H. Tang, "A pore morphological study of gas-atomized Ti-6Al-4V powders by scanning electron microscopy and synchrotron X-ray computed tomography," *Powder Technology,* vol. 330, pp. 425 - 430, 2018.

[66] R. Gerling, R. Leigeb and F. Schimansky, "Porosity and argon concentration in gas atomized y-TiAl powder and hot isostatically pressed compacts," *Materials Science and Engineering A,* vol. 252, pp. 239 - 247, 1998.

[67] B. Rabin, G. Smolik and G. Korth, "Characterization of Entrapped GAses in Rapidly Solidified Powders," *Materials Science and Engineering: A,* vol. 124, no. 1, pp. 1 - 7, 1990.

[68] P. Shukla, R. Mandal and S. Ojha, "Non-equilibrium solidification of undercooled droplets during atomization process," *Bulletin of Materials Science,* vol. 24, no. 5, pp. 547 - 554, 2001.

[69] J. Choi, G. Shin, H. Lee, D. Yang, S. Yang, C. Lee, M. Brochu and J. Yu, "Evaluation of Powder Layer Density for the Selective Laser Melting Process," *Materials Transactions,* vol. 58, no. 2, pp. 294 - 297, 2016.

[70] E. Olakanmi, "Selective laser sintering/melting (SLS/SLM) of pure Al, Al-Mg, and Al-Si powders: Effect of processing conditions and powder properties," *Journal of Materials Processing Technology,* vol. 213, pp. 1387 - 1405, 2013.

[71] A. Spierings, M. Schneider and R. Eggenberger, "Comparison of density measurement techniques for additive manufactured metallic parts," *Rapid Prototyping Journal,* vol. 17, no. 5, pp. 380 - 386, 2011.

[72] B. Liu, R. Wildman, C. Tuck, I. Ashcroft and R. Hague, "Investigation of the effect of particle size distribution on processing parameters optimisation in selective laser melting process," Additive Manufacturing Research group, Loughborough, 2011.

[73] S. Brika, M. Letenneur, C. Dion and V. Brailovski, "Influence of particle morphology and size distribution on the powder flowability and laser powder bed fusion manufacturability of Ti-6Al-4V alloy," *Additive Manufacturing,* vol. 31, 2020.

[74] A. Maamoun, M. Elbestawi, G. Doscbaeva and S. Veldhuis, "Thermal post-processing of Al10SiMg parts produced by Selective Laser Melting using recycled powders," *Additive Manufacturing,* vol. 21, pp. 234 - 247, 2018.

[75] H. Tang, M. Qian, N. Liu, X. Zhang, G. Yang and J. Wang, "Effect of Powder Reuse Times on Additive Manufacturing of Ti-6Al-4V by Selective Electron Beam Melting"," *Journal of Metals (JOM),* vol. 67, no. 3, pp. 555 - 563, 2015.

[76] P. Nandwana, W. Peter, R. Dehoff, L. Lowe, M. Kirka, F. Medina and S. Babu, "Recyclability Study on Inconel 718 and Ti-6Al-4V Powders for Use in Electron Beam Melting," *Metallurgical and Materials Transactions B,* vol. 47, pp. 754 - 762, 2016.

[77] D. Bergstrom, "The Absorption of Laser Light by Rough Metal Surfaces," Lulea University of Technology, Ostersung, Sweden, 2008.

[78] I. Ursu, I. Apostol, D. Cracium, M. Dinescu, I. Mihailescu, L. Nistor, A. Popa, V. Teodorescu, A. Prokhorov and N. Chapliev, "On the influence of surface condition on air plasma formation near metals irradiated by microsecond TEA CO2 laser pulses," *Journal of Physics D: Applied Physics,* vol. 17, no. 4, 1984.

[79] A. Spierings, M. Voegtlin, T. Bauer and K. Wegener, "Powder flowability characterisation methodology for powder-bed-based metal additive manufacturing," *Progress in Additive Manufacturing,* vol. 1, pp. 9 - 20, 2016.

[80] E. Olakanmi, "Direct selective laser sintering of aluminum alloy powders," Institute for Materials Research, Leeds, 2008.

[81] A. Mullis, N. Adkins and R. Cochrane, "Estimation of Cooling Rates During Close-Coupled Gas Atomization Using Secondary Dendrite Arm Spacing Measurement," *Metallurgical and Materials Transactions B,* vol. 44, 2013.

[82] C. Meier, R. Weissbach, J. Weinberg, W. Wall and A. Hart, "Critical influences of particle size and adhesion on the powder layer uniformity in metal additive manufacturing," *Journal of Materials Processing Technology,* vol. 266, pp. 484 - 501, 2019.

[83] C. Roberts, D. Bourell, T. Watt and J. Cohen, "A novel processing approach for additive manufacturing of commercial aluminum alloys," *Physics Procedia,* vol. 83, pp. 909 - 917, 2016.

[84] D. Gu and Y. Shen, "Balling phenomena in direct laser sintering of stainless steel powder: Metallurgical mechanisms and control methods," *Materials and Design,* vol. 30, pp. 2903 - 2910, 2009.